2D Compressible Viscous-Flow Solver on Unstructured Meshes with Linear and Quadratic Reconstruction of Convective Fluxes

Interim Project Report

Master of Technology

By

Mohamed Yousuf .A .U

(**Roll No. 04410304**)

DEPARTMENT OF MECHANICAL ENGINEERING

INDIAN INSTITUTE OF TECHNOLOGY GUWAHATI

NOVEMBER-2005

CERTIFICATE

---

*This is to certify that the work contained in this thesis entitled "**Computation of Compressible, inviscid and viscous turbomachinary cascade flows on structured and unstructured meshes** " by **Mohamed Yousuf .A.U** (**04410304**), has been carried out in the Department of Mechanical Engineering, Indian Institute of Technology Guwahati under my supervision and that it has not been submitted elsewhere for a degree.*

Dr. Anoop. K. Dass

Associate Professor,

July, 2005 Dept. of Mechanical Engineering ,

Guwahati. Indian Institute of Technology Guwahati, Assam.

ACKNOWLEDGEMENT

I feel honored to express my deepest and most sincere gratitude to my thesis supervisor, Dr. Anoop. K. Dass, for his invaluable guidance, kind suggestion and encouragement throughout the progress of this work. I am highly indebted to him for providing me ample freedom to work my way and simultaneously giving me a taste of research work.

I would also like to take this opportunity to express my sense of gratitude to the other faculty members for their kind help and encouragement and to all the non-teaching staff of the department, without whose help, I would not have completed this project work.

I heartily thank my senior Gundeti Lavan kumar and Suresh Kumar for his kind suggestions and encouragement. I wish to record the help extended to me by all my friends especially to Khaja Nijamudeen, Prabodh, Tapan Mishra, Sajeed, Sunil and Vishnuvardhana Rao for their helpful discussions and encouragement. Also I would like to thank my dear friends and all my classmates for their good company during my stay at IIT Guwahati. I would also like to thank all the members of my family for their tremendous support and love all through.

November 13, 2005

Contents

List of Figures

Nomenclature

c	Speed of sound
C_d	Coefficient of drag
C_l	Coefficient of lift
C_p	Coefficient of pressure
dS	Surface formed by the boundary of the control volume
$d(c)$	Degree of a cell (number of faces bounding the face)
e	Specific energy
F, G	Vector of conservative fluxes in the x and y directions
H	Total enthalpy
M	Mach number
n_x, n_y	Direction cosines of the unit outward normal to the interface
p	Pressure
Q	Source term
R_1, R_2, R_3	Riemann invariants
$\vec{S}$	Surface vector
t	Time
U	Vector of conserved variables
u, v	Cartesian components of the velocity vector
V	Velocity vector
x, y	Cartesian components
$\triangle t$	Time step
$\triangle x, \triangle y$	Spatial mesh step in x, y directions
$\overrightarrow{\nabla} U$	Gradient vector of the conserved variables
$\overrightarrow{\nabla} r$	Distance vector

Greek Letters

Ω	Control volume
ρ	Density
γ	Specific heat ratio
α	Angle of attack

Subscript

c	Centroid of cell
f	Fictitious state
I	Interior state
L, R	Left and right states
$\parallel$	Component parallel to the interface of the control volume side
x	Component in x directioin
$\perp$	Component perpendicular to the control volume side

Superscript

$+$	Positive
$-$	Negative
t	Time step

AGARD:	Advisory Group for Aerospace Research and Development
GAMM:	German Association for Applied Mathematics and Mechanics
NACA:	National Advisory Committee for Aeronautics (NASA)
NASA:	National Aeronautics and Space Administration
NACA 0012:	12 thick symmetrical airfoil
VKI:	Von Karman Institute

Abstract

This work is mainly concerned with the enhancement of the finite volume code for computation of compressible viscous and inviscid flows. As the code is intended to be somewhat general in nature and it is based on unstructured grid data structure. The code can be used for or adapted to any new geometry just by making minor changes in preprocessor (and without touching the solver). The inviscid part of the code is validated by extensive comparison with single NACA 0012 airfoil flow, bump in a channel flow and staggered biplane flow results. The viscous part is validated by solving a staggered biplane airfoil problem. The accuracy of the solver is uplifted by quadratic reconstruction.

Chapter 1

Introduction

1.1 Motivation and Aim

The history of Computational Fluid Dynamics started in the early 1970's. Around that time, it became an acronym for a combination of physics, numerical mathematics, and, to some extent, computer sciences employed to simulate fluid flows. The beginning of CFD was triggered by the availability of increasingly more powerful mainframes and the advances in CFD are still tightly coupled to the evolution of computer technology. Among the first applications of the CFD methods was the simulation of transonic flows based on the solution of non-linear potential equation. Thanks to the rapidly increasing speed of supercomputers and due to the development of a variety of numerical schemes and acceleration techniques, it was possible to compute inviscid flows past complete aircraft configurations or inside of turbomachines. With the mid 1980's, the focus started to shift to the significantly more demanding simulation of viscous flows governed by the Navier-Stokes equations.

Due to the steadily increasing demands on the complexity and fidelity of flow simulations, grid generation methods had to become more and more sophisticated. The

development started first with relatively simple structured meshes constructed either by algebraic methods or by using partial differential equations. But with increasing geometrical complexity of the configurations, the grid had to be broken into a number of topologically simpler blocks. However, the generation of a structured, multiblock grid for a complicated geometry may still take weeks to accomplish. Therefore, the research also focused on the development of unstructured grid generators (and flow solvers), which promise significantly reduced setup times, with only a minor user intervention. Nowadays, CFD methodologies are routinely employed in the fields of aircraft, turbomachinery, car and ship design. Furthermore, CFD is also applied in meteorology, oceanography, astrophysics, in oil recovery, and also in architecture.

The present work aims to analyze the compressible flow field for transonic and supersonic cases. A cell-centered finite volume method is used to solve 2D Euler and Navier-Stokes equations on unstructured meshes. The solution accuracy of solver is improved by implementing quadratic reconstruction.

1.2 Literature Review

The concept of using arbitrary control volumes to solve numerically the conservation laws was established in the late 70's. Jameson and Mavriplis [1] reported some of the earliest results from solving the 2D Euler equations on regular triangular grids that were obtained by subdividing the quadrilateral grids. Their work is an extension of what was established for finite volume schemes on structured grids to triangular mesh, in a cell-centered framework. Godunov [2] introduced a high level physics in the discretization procedure by solving the Riemann problem at cell interfaces. The solution is considered *constant* in each control volume and equal to the cell-averages. The resolution of such Riemann problems remains however complex

and time consuming. Moreover, the averaging procedure at each time step causes loss of many information. Therefore the problem is usually not solved exactly. On the contrary, approximate forms are considered. Roe scheme [3] is one of the most popular approximate Riemann's solvers. This is based on characteristic decomposition of flux difference while ensuring the conservation property of the scheme. This scheme has shown to be very accurate and particularly suited for explicit upwind formulation. However, it suffers from *carbuncle phenomenon* at high Mach numbers.

Making use of similarity transformations and homogeneity property of Euler equations, Steger and Warming [4] split the flux depending on the sign of eigen values of the flux Jacobian matrix. This splitting method produces errors at sonic point and stagnation point due to *discontinuity in flux Jacobian* at these points. van Leer [5] proposed an alternative splitting, which gives noticeably better results and resolves steady shock profiles in at most two zones. For solving contact discontinuities and shear layers the FVS schemes, however, exhibited a serious disadvantage by having excessive *numerical dissipation* leading to significant errors in viscous calculations

In another effort to develop less dissipative upwind schemes, introducing the flavor of the FDS scheme into FVS scheme reduces the surplus dissipation of the FVS. In the 90's, the new schemes are introduced to overcome the difficulties in earlier methods. One is the AUSM (Advection Upstream Splitting Method) proposed by Liou and Steffen [6] in 1993. This scheme is robust and converges as fast as the Roe splitting. Even though the scheme, AUSM, enjoys remarkable success, *post shock overshoot* and a *glitch* in the slowly moving shock are the drawbacks in AUSM scheme. As a result, a new version, termed AUSM+, has been derived and is shown in Liou paper [7].

Jameson [8] brought significant development in time marching methods using Runge-

Kutta time marching technique. He demonstrated that the convergence of a time dependent hyperbolic system to a steady state can be substantially accelerated by the introduction of multiple grids. Barth and Jesperson [9] introduced a novel upwind scheme for the solution of Euler equations on unstructured meshes. This scheme first performs a linear reconstruction to interpolate data to the control volume faces and then employs an approximate Riemann solver to compute the fluxes. Limiting function is introduced to *preserve monotonicity*.

Based on the work of Barth and Fredrickson [10], Barth developed the concept of K- exact reconstruction scheme [11], i.e., a reconstruction exact for a polynomial of degree k. The polynomial in Barth's method is defined in a way which guarantees the conservation of the mean. Delanaye and Essers [12] developed a particular form of quadratic reconstruction for the cell-centered scheme which is computationally more efficient than the method of Barth.

1.3 Organization of Report

The report has been organized in 5 chapters and the outline is as follows: Chapter 2 presents the governing equations and upwind schemes. Chapter 3 gives an idea about finite volume technique and its formulations for solution of 2-D Navier-Stokes equations. Besides that the boundary conditions are also discussed in this chapter. In chapter 4 the inviscid and viscous part of the code are validated. Chapter 5 mentions about conclusions and future flow path of the project.

Chapter 2

Governing Equations and Upwind Schemes

2.1 2D Navier-Stokes equations

Conservation form of 2D compressible, Navier-Stokes equations can be written in form of a vector of conservative variables $\vec{U}$ and two flux vectors $\vec{F}$ and $\vec{G}$. $\vec{F_I}$ and $\vec{G_I}$ are the vectors of convective or inviscid terms and $\vec{F_V}$ and $\vec{G_V}$ are the vectors of viscous terms. In absence of source terms nondimensional form of compressible Navier-Stokes equations can be written as

$$\frac{\partial U}{\partial t} + \frac{\partial (F_I - F_V)}{\partial x} + \frac{\partial (G_I - G_V)}{\partial y} = 0 \tag{2.1.1}$$

$$U = \begin{bmatrix} \rho \\ \rho u \\ \rho v \\ e \end{bmatrix} F_I = \begin{bmatrix} \rho u \\ \rho u^2 + p \\ \rho uv \\ (e+p)u \end{bmatrix} \quad G_I = \begin{bmatrix} \rho v \\ \rho vu \\ \rho v^2 + p \\ (e+p)v \end{bmatrix} \tag{2.1.2}$$

$$F_V = \frac{1}{Re_L}\begin{bmatrix} 0 \\ \tau_{xx} \\ \tau_{xy} \\ u\tau_{xx} + v\tau_{xy+} - q_x \end{bmatrix} \quad G_V = \frac{1}{Re_L}\begin{bmatrix} 0 \\ \tau_{xy} \\ \tau_{yy} \\ u\tau_{xy} + v\tau_{yy} - q_y \end{bmatrix} \tag{2.1.3}$$

$$\tau_{xx} = 2\mu\frac{\partial u}{\partial x} - \mu\frac{2}{3}\left(\frac{\partial u}{\partial x} + \frac{\partial v}{\partial y}\right) \quad \tau_{yy} = 2\mu\frac{\partial v}{\partial y} - \frac{2}{3}\mu\left(\frac{\partial u}{\partial x} + \frac{\partial v}{\partial y}\right) \quad \tau_{xy} = \mu\left(\frac{\partial u}{\partial y} + \frac{\partial v}{\partial x}\right) \tag{2.1.4}$$

$$q_x = -\frac{\mu}{(\gamma-1)M_\infty^2 Pr}\frac{\partial T}{\partial x} \qquad q_y = -\frac{\mu}{(\gamma-1)M_\infty^2 Pr}\frac{\partial T}{\partial y} \tag{2.1.5}$$

The nondimensionalization carried out using freestream variables ρ_∞, U_∞ and T_∞. M_∞ *is* U_∞/c_∞. Reynolds number defined based on characteristic length $Re_L = \rho_\infty U_\infty L/\mu_\infty$. Prandtl number is taken as 0.72. For mathematical closure of the equations we use the equation of state

$$p = \rho RT \tag{2.1.6}$$

e is the sum of internal energy and kinetic energy given as

$$e = \rho C_v T + \frac{1}{2}\rho(u^2 + v^2) \tag{2.1.7}$$

μ is nondimensionalized using Sutherland's law

$$\frac{\mu}{\mu_\infty} = \left(\frac{T}{T_\infty}\right)^{\frac{3}{2}}\frac{T_\infty + S1}{T + S1} \tag{2.1.8}$$

$S1$ is the Sutherland's constant 110. If viscous terms are set to zero, then the equation is transformed to a 2D unsteady compressible inviscid flow equations.

2.2 Upwind schemes

The system of compressible Navier-Stokes equations are second order partial differential equations. These equations are parabolic-hyperbolic in time and space but a mixed elliptic-hyperbolic nature in space for stationary formulation. As described in section 2.1, the Navier-Stokes equations can be split into convective and viscous terms. The unsteady compressible inviscid flow equations are hyperbolic in nature and viscous terms are elliptic in nature. We need special attention for the inviscid equations. The property of nonlinear hyperbolic system of equations allow discontinuities in the solution even if the initial data is smooth. Numerical methods which need the mathematical continuity assumption may not predict these discontinuities present in the solution accurately. Hence when defining numerical methods for such equations physical propagation of perturbations, along characteristics should be considered. The schemes which consider physical properties of the flow equations are popularly known as upwind schemes. Central schemes require lower numerical effort or less CPU time for evaluation. But these schemes do not consider the characteristic wave information direction and hence poor accuracy at discontinuities.

Upwind differencing represents an attempt to include our knowledge of the character of the equations in our difference expressions. The basic idea behind upwinding was first proposed in a landmark paper by Courant, Isaacson and Rees [15]. Their paper dealt with the one-dimensional linear advection equation and proposed taking one-sided differences based on the sign of the wave speed. In an upwind formulation, there are two states on either side of a face which must be resolved into a single value for the flux through the face.

Upwind schemes roughly divided into four main groups.

1. Flux vector splitting
2. Flux difference splitting
3. Total variation diminishing (TVD)

4. Fluctuation splitting

1. Flux vector splitting

One class of flux vector splitting (FVS) scheme decomposes the vector of the convective fluxes in to two parts according to the sign of certain characteristic variables, which are in general similar to but not identical with eigenvalues of the convective flux Jacobian. The two parts of the flux vector are then discretized by upwind biased differences. The very first FVS schemes of this type developed in the beginning by Steger and Warming and van Leer, respectively. Second class of FVS schemes decompose the flux vector into a convective and a pressure (an acoustic) part. This idea is utilized by schemes like AUSM (*Advection Upstream Splitting Method*) of Liou et al [6], or CUSP scheme (*Convective Upwind Split Pressure*) of Jameson [16] respectively. The second group of FVS schemes gained recently larger popularity particularly because of their improved resolution of shear layers with only moderate computational effort. An advantage of FVS schemes is also that they can easily extended to real gas flows, as opposed to flux difference splitting or TVD schemes.

2. Flux difference splitting

Flux difference splitting schemes evaluate the convective fluxes at a face of control volume from the *left* and *right* state by solving Riemann (shock tube) problem. The idea to solve Riemann problem was first introduced by Godunov [2]. In order to reduce numerical effort required for exact solution of Riemann problem, *approximate* Riemann solvers was developed, e.g., Roe [3] and Osher et al [17].

3. TVD Schemes

The idea of TVD schemes first introduced by Harten in 1983. The TVD schemes based on concept aimed at preventing the generation of new extrema in flow solution. The principal condition for a TVD scheme are that maxima must be non increasing,

minima non decreasing and no new local extrema may be created. Such scheme is called *monotonicity preserving*. This property allows to resolve a shock wave without any spurious oscillations of solutions. The disadvantage of TVD scheme is that they can not easily extended to higher than second order accuracy. This limitation can be overcome using ENO (*Essentially Non-Oscillatory*) discretization scheme.

4. Fluctuation splitting

Fluctuation splitting provides true multi dimensional upwinding. All upwind schemes split the equation according to orientation of grid cells. But fluctuation splitting schemes aims at resolve flow features which are not aligned with the grid. The flow variables are associated with the grid nodes. Intermediate residuals are computed as flux balances over the grid cells, which consists of triangles in 2D and tetrahedra in 3D. The cell based residuals are then distributed in an upwind biased manner to all the nodes. After that the solution is updated using nodal values. So far these schemes are used only in research codes. This can be attributed to the complexity and high numerical effort, as well as to convergence problems.

2.3 Basic principles of upwind discretization

The one dimensional wave equation is given by

$$\frac{\partial U}{\partial t} + c\frac{\partial U}{\partial x} = 0 \tag{2.3.9}$$

Courant discretized the wave equation based on the sign of eigenvalue c. for $c > 0$

$$\frac{{U_i}^{n+1} - {U_i}^n}{\triangle t} + c\frac{{U_i}^n - {U_{i-1}}^n}{\triangle x} = 0 \tag{2.3.10}$$

or

$$U_i{}^{n+1} = U_i - \lambda(U_i{}^n - U_{i-1}{}^n) \tag{2.3.11}$$

where $\lambda = c\frac{\triangle t}{\triangle x}$ is the Courant number. The truncation error is $c\frac{\triangle x}{2}(1-\lambda)U_{xx}$ and is order of $(\triangle t, \triangle x)$. This explicit scheme is first order accurate , so there is only one unknown, $U_i{}^{n+1}$ at any level n. The scheme is conditionally stable. for $0 < \lambda < 1$, but unstable for negative characteristic speeds. For negative propagation speeds $c < 0$, the following one-sided backward space difference scheme is stable.

$$U_i{}^{n+1} = U_i - \lambda(U_{i+1}{}^n - U_i{}^n) \tag{2.3.12}$$

The schemes given by equations (2.3.10) and (2.3.12) are known as upwind schemes. The schemes are applied in discretization procedure based on the direction of propagation of wave. For $c > 0$ wave equation can be solved by prescribing a physical boundary condition at left side, i=1, and no numerical conditions are required at the downstream end of the domain. Exactly the reverse holds good for scheme given by equation (2.3.12), which will be solved by sweeping the mesh from right to left and no numerical condition is required at i=1. The CIR upwind scheme which is valid for any sign of c is given by

$$\frac{U_i^{n+1} - U_i^n}{\triangle t} + \frac{c+|c|}{2}\frac{U_i{}^n - U_{i-1}{}^n}{\triangle x} + \frac{c-|c|}{2}\frac{U_{i+1}{}^n - U_i{}^n}{\triangle x} = 0 \tag{2.3.13}$$

2.4 Flux-vector splitting schemes

The idea behind the flux-vector splitting schemes is to divide the flux vector into positive and negative components based on the eigen value structure of the Jacobian matrix. This formulation is based on the fact that the fluxes are homogeneous functions of degree one in U.

2.4.1 van Leer's flux-vector splitting (FVS)

First flux-vector splitting scheme introduced by Steger and Warming in 1981. But it suffers from sonic glitch problem. van Leer introduced a flux splitting scheme by imposing certain number of conditions on F^+ and F^- such that the associated Jacobians are continuous functions of Mach number and expressed as polynomial of the lowest possible order. In addition eigen values numerical flux functions of $F(U)^+$ must be positive or zero and those of $F(U)^-$ negative or zero, with one eigen value equal to zero in subsonic range $|M| < 1$. van Leer flux expressions are

$$F_\perp = \begin{bmatrix} \rho u_\perp \\ \rho u_\perp u + p n_x \\ \rho u_\perp v + p n_y \\ \rho u_\perp H \end{bmatrix} \tag{2.4.14}$$

$$F_\perp^\pm = \pm \frac{\rho c (1 \pm M_\perp)^2}{4} \begin{bmatrix} 1 \\ u \pm (-M_\perp \pm 2)\frac{c}{\gamma} n_x \\ v \pm (M_\perp \pm 2)\frac{c}{\gamma} n_y \\ \frac{q^2 - u_\perp^2}{2} + \frac{c^2}{2(\gamma+1)}[(\gamma-1)M_\perp \pm 2]^2 \end{bmatrix} \tag{2.4.15}$$

If $M_\perp \geq 1$, then $F_\perp^+ = F_\perp, F_\perp^- = 0$

If $M_\perp \leq -1$, then $F_\perp^- = F_\perp, F_\perp^+ = 0$

If $-1 > M_\perp > 1$,then $F_\perp^+ = F_\perp^+(U_L) + F_\perp^-(U_R)$

Flux vector splitting scheme of van Leer performs very well in case of Euler equations. The simplicity and robustness and easy implementation are main advantages of this scheme. But in case of Navier-Stokes equations splitting errors in in momentum an energy equation smear out the boundary layers and also lead to inaccurate stagnation and wall temperatures.

2.4.2 Roe's flux-difference splitting (FDS)

Roe's flux-difference splitting solves an approximate Riemann problem at the cell interface [3]. The left and right states of the interfaces are connected by a path in phase space that is composed of a set of discrete waves, with uniform states between the cells. This then provides a means of forming the flux at the intermediate state yielding the upwinded flux. That is, if the flux is linearized about left state

$$\tilde{F}(U_L, U_R) = F(U_L) + \Delta F^- \tag{2.4.16}$$

and then the right,

$$\tilde{F}(U_L, U_R) = F(U_R) - \Delta F^+ \tag{2.4.17}$$

then sum these and divided by two, the numerical flux is obtained as

$$\tilde{F} = \frac{1}{2}(F(U_L) + F(U_R)) - \frac{1}{2}(\Delta F^+ - \Delta F^-) \tag{2.4.18}$$

The flux differences are written in terms of the upwinded flux Jacobians, formed at an undetermined intermediate state, $\hat{U}$

$$\Delta F^+ = \hat{A}^+ \Delta U, \qquad \Delta F^- = \hat{A}^- \Delta U$$

Combining this into (2.4.18) yields the upwind flux as

$$\tilde{F} = \frac{1}{2}(F_L + F_R) - \frac{1}{2}|\hat{A}|(U_R - U_L) \tag{2.4.19}$$

In practice, the dissipation matrix is computed in terms of the eigenvalues and eigenvectors of the flux Jacobian evaluated at the intermediate state, and the change in the Riemann invariants about the intermediate state. then the flux is written as

$$\tilde{F} = \frac{1}{2}(F_L + F_R) - \frac{1}{2}\sum_{i=1}^{4} |\hat{c}_i| \Delta \hat{V}_i \hat{R}_i \tag{2.4.20}$$

The intermediate state is formed as

$$\begin{aligned}
\hat{\rho} &= \sqrt{\rho_L \rho_R} \\
\hat{u} &= u_L\omega + u_R(1-\omega) \\
\hat{v} &= v_L\omega + v_R(1-\omega) \\
\hat{H} &= H_L\omega + H_R(1-\omega) \\
\hat{c} &= (\gamma-1)(\hat{H} - \tfrac{1}{2}(\hat{u}^2 + \hat{v}^2))
\end{aligned}$$

where

$$\omega = \frac{\sqrt{\rho_L}}{\sqrt{\rho_L} + \sqrt{\rho_R}}$$

The eigenvalues, $\hat{\lambda}_i$, at the intermediate state are

$$\hat{\lambda} = \begin{bmatrix} \hat{u}_c - \hat{c} \\ \hat{u}_c \\ \hat{u}_c \\ \hat{u}_c + \hat{c} \end{bmatrix}$$

While the change in the characteristic variables about the intermediate state, $\Delta\hat{V}_i$ are

$$\Delta\hat{V}_i = \begin{bmatrix} \frac{(\Delta P - \hat{\rho}\hat{c}\Delta u_c)}{2\hat{c}^2} \\ \frac{\hat{\rho}\Delta v_c}{\hat{c}} \\ \Delta\rho - \frac{\Delta P}{\hat{c}^2} \\ \frac{(\Delta P + \hat{\rho}\hat{c}\Delta u_c)}{2\hat{c}^2} \end{bmatrix}$$

with $\Delta(\ ) = (\ )_R - (\ )_L$. The acoustic eigenvalues, $\hat{\lambda}_{1,4}$ are modified to prevent expansion shocks, yielding the $\hat{c}_i$ as

$$\hat{c}_{2,3} = \hat{\lambda}_{2,3}$$

$$\hat{c}_{1,4} = \begin{cases} |\hat{\lambda}_{1,4}| & |\hat{\lambda}_{1,4}| \geq \frac{1}{2}\delta\hat{\lambda}_{1,4} \\ \frac{\hat{\lambda}_{1,4}^2}{\delta\hat{\lambda}_{1,4}} + \frac{1}{4}\delta\hat{\lambda}_{1,4} & |\hat{\lambda}_{1,4}| < \frac{1}{2}\delta\hat{\lambda}_{1,4} \end{cases} \tag{2.4.21}$$

where

$$\delta_i = max(4(\lambda_{i,R} - \lambda_{i,L}), 0)$$

The columns of $\hat{R}$ are the right eigenvectors of A and are formed at the intermediate state.

$$\hat{R} = \begin{bmatrix} 1 & 0 & 1 & 1 \\ \hat{u} - n_x\hat{c} & -n_y\hat{c} & \hat{u} & \hat{u} + n_x\hat{c} \\ \hat{v} - n_y\hat{c} & n_x\hat{c} & \hat{v} & \hat{v} + n_y\hat{c} \\ \hat{H} - \hat{u}_c\hat{c} & \hat{v}_c\hat{c} & \frac{\hat{u}^2+\hat{v}^2}{2} & \hat{H} + \hat{u}_c\hat{c} \end{bmatrix} \tag{2.4.22}$$

This numerical flux has been proven to be robust, can capture strong, cell-aligned shocks in one cell and, importantly, treats contact surfaces properly, yielding low dissipation across shear and boundary layers. The implementation of this flux for non-reacting, single component gases is relatively straight forward, but for reacting or non-reacting flows of multi component gases the intermediate state is not unique, and is costly to compute. Despite its few shortcomings, the numerical flux has proven to be quite useful, and is probably the most used upwind flux formula today.

2.4.3 AUSM+

Liou and Steffen proposed AUSM for 2D Euler equations, in which the cell interface advection Mach number is appropriately defined to determine the upwind extrapolation for the convective quantities. AUSM+ [7] is designed to overcome the defect of AUSM which is serious overshoots behind shock. The phenomena deteriorate

convergence and increase grid dependency. AUSM+ is able to reduce this defect in only shock aligned grids, no carbuncle phenomena, satisfaction of positivity condition, no oscillations at the slowly-moving shock, and efficiency. The AUSM+ can be written at cell-interface as follows:

$$M_{1/2} = M^{+}_{L\ /\beta=\frac{1}{8}} + M^{-}_{R\ /\beta=\frac{1}{8}} \tag{2.4.23}$$

If $(M_{1/2} \geq 0)$

$$F_{1/2AUSM+} = (M^{+}_{L|\beta=1/8} c_{\frac{1}{2}} \phi_L + M^{-}_{R/\beta=1/8} c_{\frac{1}{2}} \phi_L) + (P^{+}_{L|\alpha=3/16} P_L + P^{-}_{R/\alpha=3/16} P_R) \tag{2.4.24}$$

Otherwise

$$F_{1/2AUSM+} = (M^{+}_{L/\beta=1/8} c_{\frac{1}{2}} \phi_R + M^{-}_{R|\beta=1/8} c_{\frac{1}{2}} \phi_R) + (P^{+}_{L|\alpha=3/16} P_L + P^{-}_{R/\alpha=3/16} P_R) \tag{2.4.25}$$

Where

$$\phi = [\rho\ \rho u\ \rho v\ \rho H]^T, \quad P = P[0\ n_x\ n_y\ 0]^T$$

The split Mach number and the split pressure at the cell-interface of AUSM+ are written as follows,

$$M^{\pm}|_{\beta} = \begin{cases} \pm\frac{1}{4}(M \pm 1)^2 \pm \beta(M^2-1)^2 & |M| \leq 1 \\ \frac{1}{2}(M \pm |M|) & |M| > 1 \end{cases}$$

$$P^{\pm} = \begin{cases} \frac{1}{4}(M \pm 1)^2(2 \mp M) \pm \alpha M(M^2-1)^2 & |M| \leq 1 \\ \frac{1}{2}(1 \pm sign(M)) & |M| > 1 \end{cases}$$

The split Mach number and the speed of sound at the cell-interface of AUSM+ are defined as follows,

$$M_{L,R} = \frac{U_{L,R}}{c_{\frac{1}{2}}}, \quad c_{\frac{1}{2}} = min(\tilde{c_L}, \tilde{c_R})$$

Where

$$\tilde{c} = \frac{\dot{c}^2}{max(|U|,\ \dot{c})}, \qquad \dot{c} = \sqrt{\frac{2(\gamma-1)}{(\gamma+1)}H}$$

and U is the contravariant velocity

Chapter 3

Finite Volume Method

3.1 Introduction

The finite volume method was introduced into the field of numerical fluid dynamics independently by McDonald in 1971 and McCromac and Paullay in 1972 for the solution of two dimensional, time dependent Euler solutions. The 3D solution to Euler equations given by Rizzi and Inouye in 1973. This name is given to the technique by which the integral formulation of the conservative laws are discretized directly in the physical space. Due to direct discretization of integral form of conservation laws, the basic quantities mass, momentum and energy are conserved at the discrete level. And there is no need of transformation of grids from one coordinate system to another. FVM is very flexible. It can be implemented on structured as well as unstructured grids. This renders FVM particularly suited for complex geometries. FVM can be shown to be equivalent to a low order finite element method with less numerical effort. Because of attractive properties of FVM this method is nowadays very popular and in wide use.

3.2 The conservative discretization

Finite volume can be directly applied to integral form of governing equations .The general form of conservation laws applied on a control volume Ω for scalar quantity U and volume sources Q can be given as

$$\iiint_{\Omega} \frac{\partial U}{\partial t}\, d\Omega + \iiint_{\Omega} (\overrightarrow{\nabla}.\overrightarrow{F})\, d\Omega = \int_{\Omega} Q d\Omega \tag{3.2.1}$$

Essential significance of this formulation lies in the presence of surface integral and the fact that the time variation of U inside the volume *only depends on the surface values of the fluxes*. Let us consider a control volume shown in Fig. 3.1. Divide it into a number of control volumes, the global conservation law can be obtained by summing the conservation law of sub volumes. Fluxes are calculated at the interface of control volumes. Contribution of fluxes at each interface appears twice but with opposite signs. Indeed, for volume Ω_2 for instance, we have the contribution of fluxes

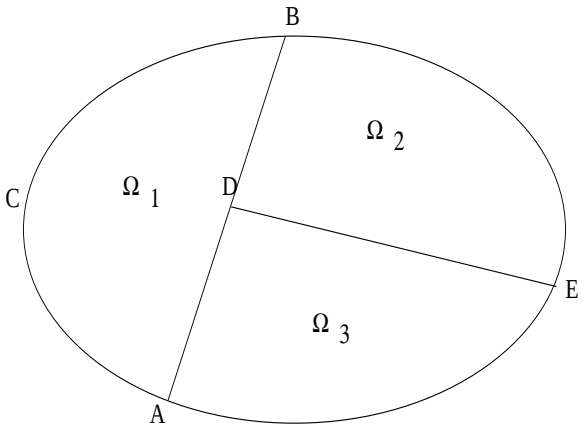

Figure 3.1: Conservation laws for subvolumes of volume Ω

$$\int_{DE} \overrightarrow{F}.d\overrightarrow{S} \tag{3.2.2}$$

while for Ω_3 we have the similar term

$$\int_{ED} \overrightarrow{F}.d\overrightarrow{S} = -\int_{DE} \overrightarrow{F}.d\overrightarrow{S} \tag{3.2.3}$$

This is the essential property to be satisfied by numerical discretization of the flux contributions, in order for scheme to be conservative.

3.3 Finite volume method

Basic concept of FVM is, the domain is subdivided into small cells (finite volumes). The conservation equations in integral form are written for each of them separately. Flux is required at the boundary of the control volume, which is a closed surface in three dimensions and a closed contour in two dimensions. This flux must be integrated to find the net flux through the boundary and source term also integrated over the control volume to evaluate time variation of U inside the control volume. Let us consider this approximation in more detail. We note that the average value of U in the cell with volume Ω is

$$\bar{U} = \frac{1}{\Omega}\int_{\Omega} U d\Omega \tag{3.3.4}$$

and the discrete form of equation 3.2.1 can be written as

$$\frac{\partial}{\partial t}(\bar{U}_j\Omega_j) + \oint F.dS = Q_j\Omega_j \tag{3.3.5}$$

In order to evaluate the fluxes, which are function of U, at the control volume boundary, U can be represented within the cell by some piecewise approximation which produces the correct value of $\bar{U}$. This from of interpolation is often referred to as *reconstruction*.

The basic elements of a FVM are thus the following:

1. Given the value of $\bar{U}$ for each control volume, construct an approximation to $U(x, y, z)$ in each control volume. Using approximation, find U at each control volume boundary. Evaluate $F(U)$ at boundary. Since there is a distinct approximation to $U(x, y, z)$ in each control volume, two distinct values to the flux will generally be obtained at any point on the boundary between two control volumes.

2. Apply some strategy for resolving the discontinuity in the flux at control volume boundary to produce a single value of $F(U)$ at any point on the boundary.

3. Integrate the flux to find the net flux through the control volume boundary using some type of quadrature.

4. Advance the solution in time to obtain new values of $\bar{U}$

3.4 Different frameworks in FVM

There are generally two discretization methods used in FVM which are cell centered and cell vertex discretization. The two frameworks differ in location of control volumes with respect to mesh and the location of the flow variable.

In cell centered scheme, flow quantities are stored at the centroid of grid cells. Thus, control volumes are identical to the grid cells. When we evaluate the discretized flow equations we have to supply convective and the viscous fluxes at the faces of the cell. The fluxes are calculated by average of fluxes computed from the values at centroids of the grid cells to the left and to the right of the cell face, but using the same face vector(usually only for convective fluxes) or by using an average of variables associated with the centroids of the grid cells to the left and to the right of the cell face or reconstructed separately on both sides of cell face from the values in the surrounding cells.

In cell vertex scheme, flow variables are stored at the grid points. The control volume

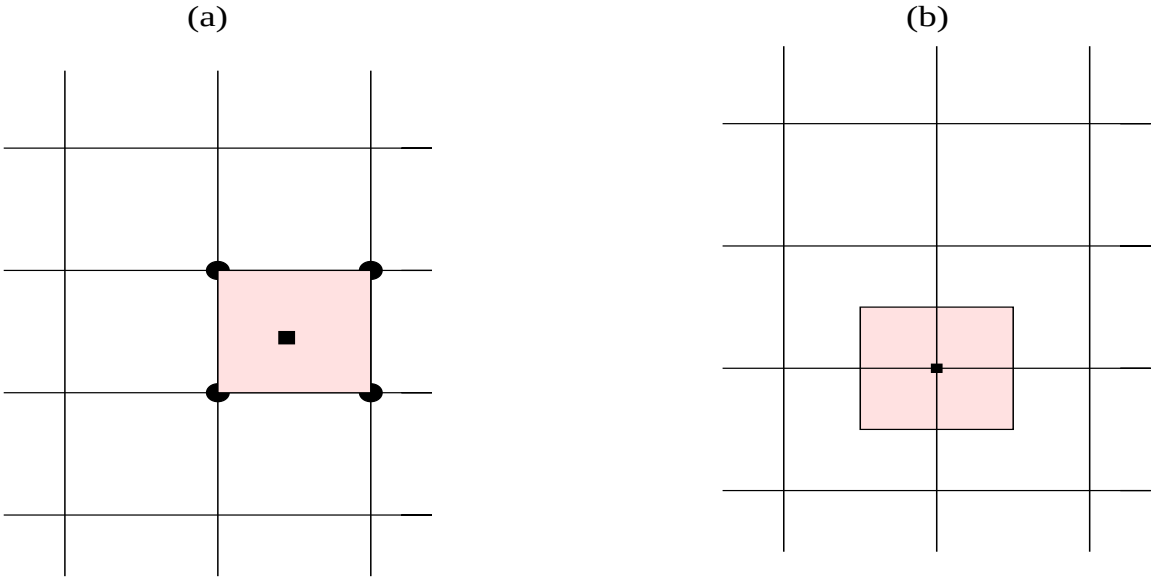

Figure 3.2: (a) Cell centered , (b) Cell vertex (median dual) finite volume methods

can be either union of all cells sharing the grid point, or some volume centered around a grid point. The former case is known as *overlapping* control volumes and in the second case *dual* control volumes.

3.4.1 Cell-centered versus cell vertex schemes

A good comparison between these schemes is given in the text [18]. Cell vertex scheme is first order accurate on distorted grids. On cartesian or on smooth grids the cell vertex scheme is second or high order accurate depending on flux evaluation scheme. In the opposite, the discretization error of cell centered scheme depends strongly on the smoothness of the grid. In general, a cell center scheme on triangular/tetrahedral grid leads to about two/six times as many control volumes and hence degrees of freedom as median dual cell scheme and hence resulting in more unknowns compare to median dual scheme. In addition, control volumes in cell centered scheme are smaller than those in cell vertex scheme. This suggest that cell centered scheme is more accurate [19]. However residual of cell centered scheme results from much smaller number of fluxes compared to a median dual scheme. Thus

there is no clear evidence about which scheme is better. Cell center schemes need more computational work as ratio of number of faces to number of edges is more and need more memory requirements as more number of variables to be stored compared to cell vertex method. Boundary conditions implementation in cell vertex schemes require additional logic in order to assure a consistent solution at boundary points contrary to cell centered schemes; it is simple. In addition for cell vertex schemes mass flux matrix treatment is required compare to cell centered scheme.

3.5 Discretization of N-S equations

Recall the conservation form of 2D Navier-Stokes equations

$$\frac{\partial U}{\partial t} + \frac{\partial (F_I - F_V)}{\partial x} + \frac{\partial (G_I - G_V)}{\partial y} = 0 \tag{3.5.6}$$

the divergence form of N-S equation can be written as

$$U_t + \nabla.(\overrightarrow{F}_I - \overrightarrow{F}_V) = 0 \tag{3.5.7}$$

where

$$U_t = \frac{\partial U}{\partial t} \tag{3.5.8}$$

$$\overrightarrow{F_I} = F_I \widehat{n}_x + G_I \widehat{n}_y \quad \overrightarrow{F_V} = F_V \widehat{n}_x + G_V \widehat{n}_y \tag{3.5.9}$$

Integrating equation over a control volume Ω_i (Fig. 3.3) and applying Gauss divergence theorem to evaluate total flux, we have

$$\int_{\Omega_i} U_t d\Omega + \oint_{ABC} (\overrightarrow{F}.\widehat{n}) dS_i = 0 \tag{3.5.10}$$

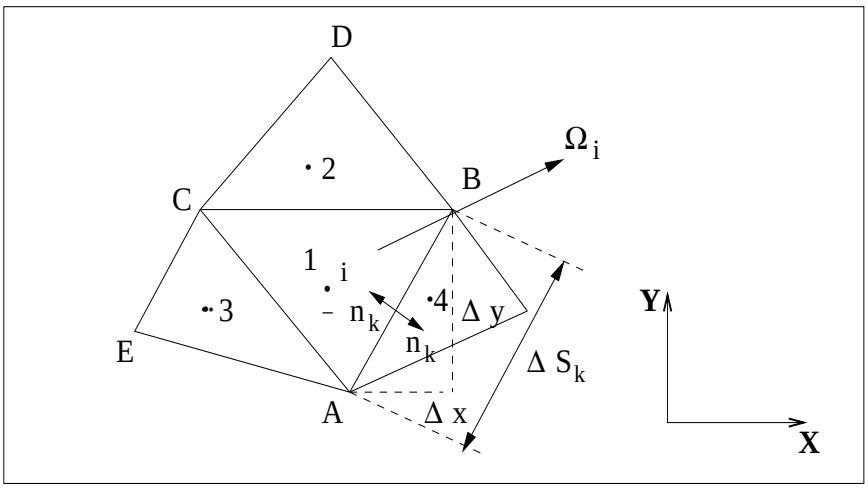

Figure 3.3: 2D finite volume method

$$\widehat{n} = \widehat{i_x} n_y + \widehat{i_y} n_y \tag{3.5.11}$$

Where, $n_x = \frac{\Delta y}{s}$, $n_y = \frac{-\Delta x}{s}$ and i is the cell number, S_i is boundary of control volume Ω_i. On integration, the space discrete form of N-S equations can be obtained as

$$\frac{d\bar{U}}{dt} + \sum_{k=1}^{3} \Big(F_{I\perp k} - F_{V\perp k} \Big) . S_k = 0 \tag{3.5.12}$$

k is the edge number. $F_{I\perp k}$ and $F_{V\perp k}$ represents normal flux on k^{th} face with $\widehat{n}$ as the unit outward normal vector for viscous and inviscid fluxes respectively. Now we arrive at the state update formula

$$\bar{U_i}^{n+1} = \bar{U_i}^{n} - \frac{\Delta t}{\Omega_i} \sum_{k=1}^{3} \Big(F_{I\perp k} - F_{V_\perp k} \Big) . S_k = 0 \tag{3.5.13}$$

where the normal flux vectors

$$F_{I\perp k} = \begin{bmatrix} \rho u_{\perp k} \\ \rho u u_{\perp k} + p n_{x,k} \\ \rho u u_{\perp k} + p n_{y,k} \\ (p+e) u_{\perp k} \end{bmatrix} \tag{3.5.14}$$

$$F_{V\perp k} = \begin{bmatrix} 0 \\ (\tau_{xx} + \tau_{xy})n_{x,k} \\ (\tau_{xy} + \tau_{yy})n_{y,k} \\ (u\tau_{xx} + v\tau_{xy} - q_x)n_{x,k} + (u\tau_{x,y} + v\tau_{yy} - q_y)n_{y,k} \end{bmatrix} \tag{3.5.15}$$

3.5.1 Discretization of viscous fluxes

In order to find the viscous fluxes F_V, the flow quantities and their first derivatives in equation (3.5.15) are to be known at the faces of control volumes. Because of elliptic nature of viscous fluxes, the values of velocity components u, v the dynamic viscosity μ, which are required for the computation of viscous terms, are simply averaged at face. Remaining task is evaluation of first derivatives of velocity and

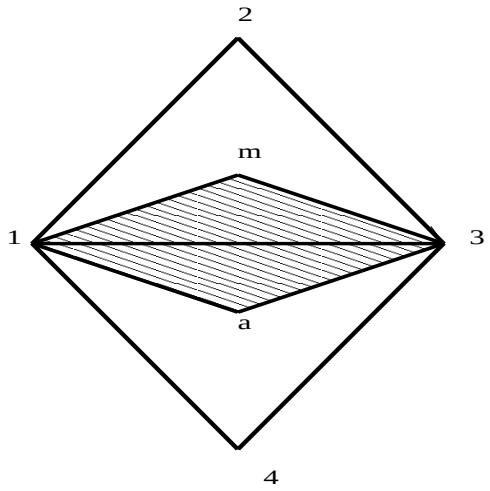

Figure 3.4: Gradient computation at faces

temperature components in viscous fluxes. Here we discuss the face-centered control volume method. An auxiliary control volume is define to evaluate the gradients at the face center. Generally control volume chosen is formed by cell vertices of the face and cell centers of left and right cells. A simple control volume is shown in Fig. 3.4. For face 13 the control volume is formed by vertices 1, 3 and cell centers m, a. Apply Green-Gauss theorem to find the gradients. Consider two triangles in Fig. 3.4 $\Delta 13m$ and $\Delta 1a3$ for which the x and y gradients can be computed using the

Green-Gauss theorem as

$$(W_x)_{13m} = \frac{1}{2A_{13m}}[W_1 y_{m3} + W_m y_{31} + W_3 y_{1m}] \tag{3.5.16}$$

$$(W_y)_{13m} = -\frac{1}{2A_{13m}}[W_1 x_{m3} + W_m x_{31} + W_3 x_{1m}] \tag{3.5.17}$$

$$(W_x)_{1a3} = \frac{1}{2A_{1a3}}[W_1 y_{3a} + W_3 y_{a1} + W_a y_{13}] \tag{3.5.18}$$

$$(W_y)_{1a3} = -\frac{1}{2A_{1a3}}[W_1 x_{3a} + W_3 x_{a1} + W_a x_{13}] \tag{3.5.19}$$

Where $y_{m3} = y_3 - y_m$, $x_{m3} = x_3 - x_m$, and so on. The next step is to obtain the face gradients. This is done using area-weighted average of these two gradients for triangles $13m$ and $1a3$:

$$(W_x)_{1a3m} = \frac{[A_{13m}(W_x)_{13m} + A_{1a3}(W_x)_{1a3}]}{[A_{13m} + A_{1a3}]} \tag{3.5.20}$$

$$(W_y)_{1a3m} = \frac{[A_{13m}(W_y)_{13m} + A_{1a3}(W_y)_{1a3}]}{[A_{13m} + A_{1a3}]} \tag{3.5.21}$$

3.6 Reconstruction and limiting

First order accurate results are obtained by assuming that the solution is constant inside each control volume. We can achieve second or high order accuracy if we assume the solution to vary over the control volumes. But it is not very easy to obtain high order accuracy in FVM. If we extend first order upwind schemes by appropriate second order accurate formulas, it leads to generation of oscillations near discontinuities. A systematic analysis of the conditions required by a scheme to give oscillation free solution was developed and initiated by Godunov, but it is proved to be first order accurate. He introduced the important concept of *monotonicity*, which

gives oscillation free solution. *Monotonicity* has the property of not allowing the creation of new extrema and does not allow unphysical discontinuities. In order to generate higher spacial approximation, the state variables at interface are obtained from the extrapolation between neighboring cell averages. This method of generation of second order upwind schemes via *variable extrapolation* is often referred as MUSCL (Monotone Upstream centered Scheme for Conservation Laws) introduced by van Leer [5].

In constructing high order schemes the assumption of piecewise constant cell distribution is replaced by linear distribution. To achieve high order accuracy unlike the calculation of interface fluxes based on the cell average values in first order schemes, flux has to be calculated based on point values on cell edges. For a given cell average values, to find the point values using reconstruction procedure we require

1. Reconstruction for obtaining point values from cell averages.

2. Accurate quadrature formula for flux integral.

Starting with cell averaged data, the solution is piecewise linearly reconstructed such that *monotonicity* condition preserved. The common cell edges, the reconstructed values are not necessarily equal as both are reconstructed from different cell averages. Thus there is a general discontinuity along common edges.

3.6.1 Multi-dimensional linear reconstruction of cell averaged data

Higher order accuracy is obtained by performing piecewise linear reconstruction of the cell averaged data. Here Barth [9] reconstruction procedure is presented. Fig. 3.5 depicts the situation for a triangle A with neighboring triangles. Linear

representation of state variables about a centroid (x_0, y_0) :

$$U(x,y) = U(x_0,y_0) + U_x(x-x_0) + U_y(y-y_0) = U(x_0,y_0) + \overrightarrow{\nabla} U.\Delta\overrightarrow{r} \quad (3.6.22)$$

$U(x_0, y_0)$ is cell average value given by state update formula equation (3.5.13). $\overrightarrow{r}$ is the distance vector, $\overrightarrow{\nabla} U$ is the best estimate of the solution gradient in the cell computed from the surrounding centroid data. U_x and U_y are the solution gradients at each cell center. We can get high order solutions by estimating the gradients via,

1. Least-square reconstruction
2. Green-Gauss reconstruction
3. Frink's higher order scheme

Least-square reconstruction

Least-square gradient reconstruction method originally formulated by Barth [10] for the derivation of high-order upwind schemes. Consider the triangular mesh shown in Fig. 3.5. Let x_i and y_i be the coordinates of node i and $U(x_0, y_0)$ be the cell average value. Now recall the equation (3.6.22)

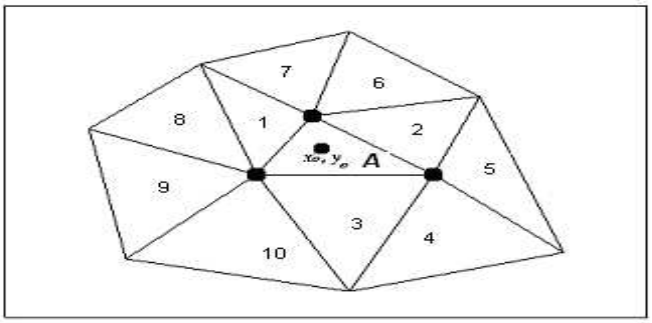

Figure 3.5: 2D triangular mesh

$$\begin{aligned} U(x,y) &= U(x_0,y_0) + U_x.(x-x_0) + U_y.(y-y_0) \\ &= U(x_0,y_0) + \overrightarrow{\nabla} U.\Delta\overrightarrow{r} \end{aligned} \tag{3.6.23}$$

let

$U_i = U(x,y)$

$U_0 = U(x_0,y_0)$

$\Delta U_i = U_i - U_0$

$\Delta x_i = x_i - x_0$

$\Delta y_i = y_i - y_0$

Now the equation (3.6.23) becomes

$$\Delta U_i = U_x \Delta x_i + U_y \Delta y_i \qquad i = 1,2,...n. \tag{3.6.24}$$

We have two unknowns U_x and U_y, and n linear equations. By minimizing the square of the error.

$$error = \sum_{i=1}^{n} (\Delta U_i - U_x \Delta x_i + U_y \Delta y_i)^2 \tag{3.6.25}$$

now we get least-square approximation of gradients as

$$U_x = \frac{||\Delta y||^2(\Delta x, \Delta U) - (\Delta x \Delta y)(\Delta y, \Delta U)}{||\Delta x||^2||\Delta y||^2 - (\Delta x_1, \Delta y)^2} \tag{3.6.26}$$

$$U_y = \frac{||\Delta y||^2(\Delta y, \Delta U) - (\Delta x \Delta y)(\Delta x, \Delta U)}{||\Delta x||^2||\Delta y||^2 - (\Delta x_1, \Delta y)^2} \tag{3.6.27}$$

Where,

$||\Delta x||^2 = \sum_{i=1}^{n} \Delta x_i^2$, $\qquad ||\Delta y||^2 = \sum_{i=1}^{n} \Delta y_i^2$

$(\Delta x, \Delta U) = \sum_{i=1}^{n} \Delta x_i \Delta U_i \qquad (\Delta y, \Delta U) = \sum_{i=1}^{n} \Delta y_i \Delta U_i$

Green-Gauss reconstruction

In this method gradients in the cell are calculated using Green's theorem.

$$\iiint_{\Omega}(\overrightarrow{\bigtriangledown}U)\,d\Omega = \int_{S}(U\overrightarrow{n})\,ds \tag{3.6.28}$$

The solution gradient for volume A is estimated by computing the boundary integral of equation (3.6.28) for some path (surface) S, surrounding volume A.

$$\overrightarrow{\bigtriangledown}U_A = \frac{1}{\Omega}\int_{S}(U\overrightarrow{n})\,ds \tag{3.6.29}$$

Frink's high order scheme using Green-Gauss reconstruction

Frink [20] applied this reconstruction method to solve 3D Euler equation. First, The gradients are evaluated using Green's theorem as

$$U_x = \frac{1}{\Omega}\int U n_y dS \tag{3.6.30}$$

$$U_y = \frac{1}{\Omega}\int U n_x dS \tag{3.6.31}$$

The above line integral is carried out around a closed path surrounding control volume. First inverse distance weighing is used to transfer the cell average data to the node as

$$U_{node} = \left(\sum_{i=1}^{N}\frac{U_i}{r_i}\right)/\left(\sum_{i=1}^{N}\frac{1}{r_i}\right) \tag{3.6.32}$$

where r_i is the distance from i-th cell center to the node of the cell and N is the total number of cells sharing the particular node. u_{node} and u_i respectively denote the values at the node and i-th cell center. Next, the trapezoidal rule is applied to

integrate around the the control volume to compute the flow gradients. For example x gradient is obtained by

$$U_x = \frac{1}{\Omega}\sum_{i=1}^{K}\left(\frac{U_{node1} + U_{node2}}{2}\right)\Delta S_k n_x \tag{3.6.33}$$

$node1$ and $node2$ are the end points of the cell face k, ΔS is the length of the cell face k, n_x is the x-component of the outward unit normal vector and K is the number of cell edges of the control volume.

in two dimensions

$$r_i = [(x_{0,i} + x_{node})^2 + (y_{0,i} + y_{node})^2]^{0.5} \tag{3.6.34}$$

Where 0 refers to cell center. Because of the relative positions and number of times each cell has been used in gradient computation (numbers enclosed in the parentheses in Fig. 3.6), the cell interface values biased toward cell A. If the state is being computed on edge 1-2 from the state and the gradient at the centroid of cell A, the interpolation utilizes information from surrounding cells on both sides of the edge, but weighted in the direction of parent cell A. Thus the procedure has the general features of three point interpolation formulas commonly used in upwind-biased structured schemes. It is computationally little bit expensive compare to earlier methods, which needed just subtraction and multiplication in the calculation of gradients in a single loop.

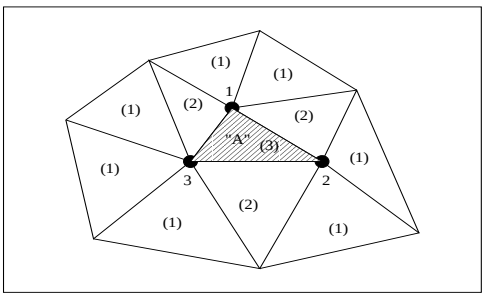

Figure 3.6: Frink's reconstruction

3.7 Quadratic-reconstruction

The fundamentals of the polynomial reconstructions to unstructured meshes for building high order upwind schemes were presented first by Barth and Fredrickson [10]. They attempted to extend to multiple dimensions some basic ideas previously developed for structured meshes. The concept of polynomial reconstruction has been applied to design essentially non-oscillatory schemes for unstructured meshes. However, the computational effort associated with these complex methods through the stencil selection turns out to be quite prohibitive for computing steady-state solutions. Moreover, the nonlinearities inherent in these techniques may produce serious convergence problems. For these reasons, Barth [11] introduced a simpler quadratic reconstruction scheme with a fixed stencil in a cell vertex finite volume solver. In the same way, a second-order finite volume solver that also preserves quadratic polynomial has been proposed by Essers et al. for structured meshes. This scheme suffers from a lack of conservation.

Our main objective is to develop a scheme whose second-order accuracy is preserved even on much distorted meshes. Delanaye and Essers [12] developed a particular form of quadratic reconstruction for the cell-centered scheme which is computationally more efficient than the method of Barth. The flux balance is performed using high order Gauss quadrature. An original quadratic reconstruction obtained by a truncated Taylor-series expansion is employed to extrapolate the flow variables at the quadrature points.

Outline of the method is the following. First, a multidimensional piecewise high order polynomial approximates the flow variables evolution in the cell. The unknowns of the control volume contour are computed. This step called as reconstruction, also can be interpreted by extrapolation. On the each edge of the mesh, the advective flux is obtained by applying a Riemann solver to reconcile the discontinuous left and right states. Time evolution is then performed after correctly integrating the flux

on the control volume contour. The spatial accuracy of the discretization depends

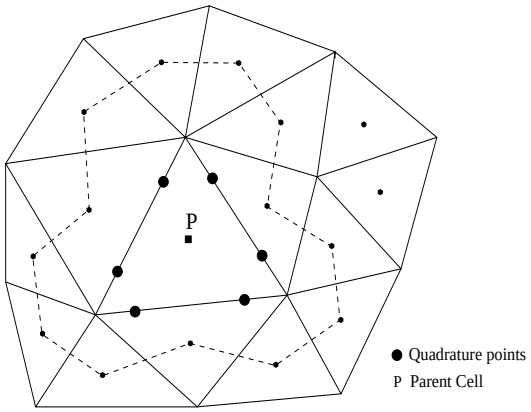

Figure 3.7: The identification of more neighbors and flux integration path showed by dashed line

on two factors;

1) The accuracy of the variables reconstruction.

2) The flux integration.

The calculation of the flux through each edge f_n^k of a parent cell in Fig. 3.7 is performed by a high order numerical integration of the flux functions using the n-points Gauss quadrature;

$$f_n^k = \delta_k \sum_{j=1}^{n} \omega_j [f(x_j^k, y_j^k) n_x^k + g(x_j^k, y_j^k) n_y^k] \tag{3.7.35}$$

Where (x_j^k, y_j^k) are the coordinates of the Gauss quadrature point j and ω_j denotes the weight associated with this point. The lucid picture about the selection of Gauss quadrature points on edges is provided in *Appendix*. By using n quadrature points, the formula (3.7.35) allows the exact integration of polynomials with degree 2n-1. Obviously, to satisfy the proposition, two quadrature points are at least required to compute exactly a flux that is a quadratic polynomial of the Cartesian coordinates. Two Riemann problems have therefore to be solved at each edge.

Right state at the quadrature point j of edge k is computed from

$$q_{R_j}^k = q_R^k + (r_j^k - r_R^k)^T \nabla q_R^k + \frac{1}{2}(r_j^k - r_R^k)^T \Re_R (r_j^k - r_R^k) \tag{3.7.36}$$

Where r is the position vector and $\Re$ the Hessian matrix of each primitive variable:

$$\Re = \begin{bmatrix} \partial^2_{xx} q & \partial^2_{xy} q \\ \partial^2_{xy} q & \partial^2_{yy} q \end{bmatrix} \tag{3.7.37}$$

If q is a quadratic polynomial of x and y, equation (3.7.36) must be exact. That requirement is met by equation (3.7.36) if the gradients and the second order derivatives in the Hessian matrix are respectively computed with a second- and first-order accuracy. This is accomplished by combining *Green-Gauss gradient* evaluation with *least-squares* based approximation of the second derivatives, which leads to a numerically efficient scheme. The technique we used to build second-order derivatives with first-order accuracy is sometimes referred to as the minimum-energy reconstruction. it simply consists in fitting a quadratic polynomial to the values of the neighboring nodes using the least-square technique. we seek to minimize the L_2 norm of the distance between a scalar function f known at the mesh nodes and a piecewise quadratic approximation f_{rec} of the latter constructed as follows:

$$f_{rec} = f_o + (r - r_o)^T \nabla f_o + \frac{1}{2}(r - r_o)^T \Re_o (r - r_o) \tag{3.7.38}$$

This is expressed by minimizing the functional

$$\sum_{i=1}^{N_\Omega} [f_{rec}(r_i) - f_i]^2 \tag{3.7.39}$$

and therefore, a N_Ω X 5 linear system has to be solved for each control volume:

$$\begin{bmatrix} \Delta x_1 & \Delta y_1 & \frac{\Delta x_1^2}{2} & \Delta x_1 \Delta y_1 & \frac{\Delta y_1^2}{2} \\ \Delta x_2 & \Delta y_2 & \frac{\Delta x_2^2}{2} & \Delta x_2 \Delta y_2 & \frac{\Delta y_2^2}{2} \\ \Delta x_3 & \Delta y_3 & \frac{\Delta x_3^2}{2} & \Delta x_3 \Delta y_3 & \frac{\Delta y_3^2}{2} \\ . & . & . & . & . \\ . & . & . & . & . \\ \Delta x_i & \Delta y_i & \frac{\Delta x_i^2}{2} & \Delta x_i \Delta y_i & \frac{\Delta y_i^2}{2} \\ . & . & . & . & . \\ . & . & . & . & . \end{bmatrix} \begin{bmatrix} u_x \\ u_y \\ u_x x \\ u_x y \\ u - yy \end{bmatrix} = \begin{bmatrix} \Delta u_1 \\ \Delta u_2 \\ \Delta u_3 \\ . \\ . \\ \Delta u_i \\ . \\ . \end{bmatrix} \tag{3.7.40}$$

where $\Delta u_i = u_i - u_0$

Finally, the quadratic reconstruction for a right state extrapolation

$$q_{R_j}^k \;=\; q_R^k + (r_j^k - r_R^k)^T \nabla^{1st} q_R^k + [-(r_j^k - r_R^k)^T \; Er_R \nabla^2 q_R^k + \frac{1}{2}(r_j^k - r_R^k)^T \Re_R (r_j^k - r_R^k)] \tag{3.7.41}$$

where ∇^{1st} is a symbol notation for the numerical gradient calculated using Green-Gaussian formula, Er_R is 2 X 3 matrix containing constant coefficients of O(h) and ∇^2 is the vector of second-order derivatives.

3.8 Limiters

Second and high order upwind discretization require use of *limiters* or *limiting functions* in order to prevent the generation of oscillations and spurious solutions in the region of high gradients (e.g., at shocks). A *limiter* is used to preserve *monotonicity* principle, i.e., the reconstructed function must not exceed the maximum and minimum of neighboring centroid values (including the centroid of parent cell) The purpose of the limiter is to reduce the high gradient used to reconstruct the left and right state at the face of the control volume in order to constrain the solution

variation. At strong discontinuities, the limiter has to reduce slopes to zero to prevent the generation of new extremum. We discuss the two limiters which are widely using

1. Limiter of Barth and Jespersen
2. Venkatakrishnan limiter

Barth and Jespersen limiter

Consider the limited form of the reconstructed function about the centroid of triangle A in Fig. 3.5.

$$U(x,y) = U(x_0,y_0) + \phi_A \overrightarrow{\nabla} U_A.\Delta\overrightarrow{r_A}, \qquad \phi_A \in [0,1] \tag{3.8.42}$$

the idea is to find the largest admissible ϕ_A. First compute U_A^{min}=min$(U_A, U_{neighbors})$ and U_A^{max}=max$(U_A, U_{neighbors})$ then require that

$$U_A^{min} \leq U(x,y)_A \leq U_A^{max} \tag{3.8.43}$$

For cell centered method, $U_{neighbors}$ are the number of cells sharing with common edge of parent cell. For linear reconstruction, extrema in $u(x,y)_A$ occurs at the vertices of the cell and the sufficient conditions stated in (3.8.43) can be easily obtained. For each vertex of the cell compute $U_i = U(x_i, y_i), i = 1, 2, 3..., d(c)$ to determine the limited value, ϕ_A, which satisfies (3.8.43).

$$\phi_A = \begin{cases} min(1, \frac{U_A^{max} - U_A}{U_i - U_A}), & \text{if } U_i - U_A > 0 \\ min(1, \frac{U_A^{min} - U_A}{U_i - U_A}), & \text{if } U_i - U_A < 0 \\ 1 & \text{if } U_i - U_A = 0 \end{cases} \tag{3.8.44}$$

with ϕ_A=min$(\bar{\phi_{A1}}, \bar{\phi_{A2}}, \bar{\phi_{A3}}, ...\bar{\phi_{Ad(c)}})$, ensures that the linearly reconstructed state variables satisfy the monotonicity principle when evaluated anywhere within a cell. Barth limiter ensures monotonicity, but it was shown to stall the convergence to steady state [21], which could be due to the use of non-differentiable functions such as max and min, apart from clipping smooth extrema.

Venkatakrishnan limiter

Venkatakrishnan limiter is widely used because of it's superior convergence properties. It is based on Barth and Jesperson monotonicity principle on unstructured grids. He modified the Van Albada limiter which is defined only for structured grids and it is continuously differentiable. The limiter reduces the reconstructed gradient ∇U at cell center i by factor

$$\phi_A = \begin{cases} \frac{1}{\Delta_2}\left[\frac{(\Delta_{1,max}^2+\epsilon^2)\Delta_2+2\Delta_2^2\Delta_{1,max}}{\Delta_{1,max}^2+2\Delta_2^2+\Delta_{1,max}\Delta_2+\epsilon^2}\right], & \text{if } \Delta_2 > 0 \\ \frac{1}{\Delta_2}\left[\frac{(\Delta_{1,min}^2+\epsilon^2)\Delta_2+2\Delta_2^2\Delta_{1,min}}{\Delta_{1,min}^2+2\Delta_2^2+\Delta_{1,min}\Delta_2+\epsilon^2}\right], & \text{if } \Delta_2 < 0 \\ 1, & \text{if } \Delta_2 = 0 \end{cases} \tag{3.8.45}$$

Where

$\Delta_{1,max} = U_{max} - U_i$

$\Delta_{1,min} = U_{min} - U_i$

$\Delta_2 = U_i - U_A$

U_{max}, U_{min} values stand for the maximum and minimum values of all surrounding cells which are shared by edges including cell i. Definitions of U_{max} and U_{min} are same as explained in previous section. Parameter ϵ^2 is intended to control the amount of limiting . Setting ϵ^2 to zero results in full limiting. Contrary to that, if ϵ^2 set to large value, the limiter function will return a value of one. Hence, there will

be no limiting at all and wiggles could occur in solution. In practice it was found that ϵ^2 should be proportional to a local length scale, i.e.,

$$\epsilon^2 = (K\Delta h)^3 \tag{3.8.46}$$

where K is a constant, and of order 1. Δh is cube-root of the volume in 3D or square root of area in 2D of the control volume. So far we have discussed Barth and Jesperson [9] limiter and Venkatakrishnan [21] limiter. Venkatakrishnan's limiter as described in above section, helps in improving convergence characteristics of original limiter, which however comes at the expense of compromising on monotonicity. Also convergence seems to be strongly influenced by the parameter, which controls the degree of limiting. This is function of an estimate of average grid size and a arbitrary constant which is found after conducting experiments for each problem. This is a limitation for Venkatakrishnan limiter to apply it in a general purpose problem.
In case of structured grids van Leer and van Albada limiters are quite successful which are continuously diffentiable. Some attempts are made, to make some changes to van Albada limiter to apply in unstructured grids. Indeed Venkatakrishnan limiter is modified form of van Albada limiter. One more attempt was made by Van Rosendale [22] on triangular meshes, weighted average of gradients at the three vertices of cell as computed by applying Green-Gauss theorem to surrounding cell center data. The limited gradient within the cell obtained by taking the weighted average of three representative gradients.

$$\nabla U_m^l \;=\; \omega_1 \nabla U_1 + \omega_2 \nabla U_2 + \omega_3 \nabla U_3 \tag{3.8.47}$$

1, 2 and 3 are cell vertices and m is parent cell. ω_1, ω_2 and ω_3 are weights given by multi dimensional limiter function based on gradients of cell vertices and ∇U_1, ∇U_2, and ∇U_3 are unlimited gradients which are combined to produce the limited gradient ∇U_m^l. This is reverse the sequence of operations employed by Frink, which is described in earlier sections.

3.9 Jawahar and Kamath limiter

Jawahar and Kamath [13] developed a new limiter similar to Van Rosendale limiter. Instead of considering the gradients at cell vertices, cell centered gradients of neighbors are considered in their computation. It involves the prescription of weights as

$$\omega_a(g_a, g_b, g_c) = \frac{g_b g_c + \varepsilon^2}{g_a^2 + g_b^2 + g_c^2 + 3\varepsilon^2} \tag{3.9.48}$$

$$\omega_b(g_a, g_b, g_c) = \frac{g_a g_c + \varepsilon^2}{g_a^2 + g_b^2 + g_c^2 + 3\varepsilon^2} \tag{3.9.49}$$

$$\omega_c(g_a, g_b, g_c) = \frac{g_a g_b + \varepsilon^2}{g_a^2 + g_b^2 + g_c^2 + 3\varepsilon^2} \tag{3.9.50}$$

Where $g_a = \|\nabla U_a\|_2^2$, $g_b = \|\nabla U_b\|_2^2$, $g_c = \|\nabla U_c\|_2^2$. The limited gradient is obtained as

$$\nabla U_m^l = \omega_a \nabla U_a + \omega_b \nabla U_b + \omega_c \nabla U_c \tag{3.9.51}$$

a, b and c are neighboring cells. They claimed that even though it may appear as minor modification in weights, implementation procedure differs significantly from that of Van Rosendale [22] equation (3.8.47) in choice of gradients for constructing the limiter. It is also appropriate to compute limiter based on neighboring cells instead of vertex gradients, as MUSCL finite volume formulation interacts with it neighbours at common interface.

3.10 Multistage time stepping

High order accuracy is obtained by multistage time integration. This method is developed by Jameson [23]. Runge-Kutta time step is used to increase the accuracy

of time integration. A fourth order time accurate solution can be obtained by

$$\begin{aligned} U_i^0 &= U_i^n \\ U_i^1 &= U_i^n - \alpha_1 \Delta t R(U_i^0) \\ U_i^2 &= U_i^n - \alpha_2 \Delta t R(U_i^1) \\ U_i^3 &= U_i^n - \alpha_3 \Delta t R(U_i^2) \\ U_i^{n+1} &= U_i^n - \alpha_4 \Delta t R(U_i^3) \end{aligned} \tag{3.10.52}$$

Where

$\alpha_1 = \frac{1}{4}$ $\alpha_2 = \frac{1}{3}$ $\alpha_3 = \frac{1}{2}$ $\alpha_4 = 1$

R is the residual.

3.11 Boundary conditions

The imposition of precise boundary conditions is of extreme significance in obtaining an accurate numerical solution. Specification of inappropriate boundary conditions may cause instabilities or it may give rise to undesirable physical and numerical waves that destroy the solution. Therefore, care must be taken while implementing the boundary conditions for a fluid flow problem, to avoid the possibility of turning into an ill-posed problem. Boundary conditions can be classified into two types - physical and numerical. Poinsot and Lele in 1992, distinguished between these two classes mentioning that a boundary condition is physical when it specifies the known physical behavior of one or more of the dependent variables at the boundaries and that it is numerical or soft when no explicit boundary condition fixes one of the dependent variables, but the numerical scheme requires an explicit specification about variables (Yee in 1981). The appropriate conditions can therefore be imposed at the boundaries of the flow domain, depending on the boundary type and the flow regime. The number of physical boundary conditions at a boundary should be equal to the number of incoming characteristics. The number of physical or numerical boundary

conditions to be imposed at boundary surface is determined by characteristic properties. The eigenvalues of Jacobian matrix are $\overrightarrow{v}.\overrightarrow{1_n}$, $\overrightarrow{v}.\overrightarrow{1_n}$, $\overrightarrow{v}.\overrightarrow{1_n} + c$, $\overrightarrow{v}.\overrightarrow{1_n} - c$. The number of physical boundary conditions depends on sign of eigenvectors.

3.11.1 Inviscid or slip wall boundary condition

Accuracy of results not only depends on the scheme applied but also depends on the treatment of wall boundary conditions. Accurate calculation of lift and drag coefficients are much important in design of aerodynamic vehicles. Detailed explanation of wall boundary condition on structured meshes can be found in [24]. Idea of implementing wall boundary conditions on unstructured meshes in both cell centered and cell vertex finite volume methods for inviscid flow are discussed in [25]. Implementation of the boundary condition is straight forward for cell vertex discretisation scheme as reference points of cell fall on the boundary.

Pressure extrapolation boundary condition

On solid walls there is no flow normal to the the boundary i.e.,

$$\overrightarrow{v}.\overrightarrow{n} = 0 \tag{3.11.53}$$

Consequently vector of convective fluxes reduces to pressure term alone, i.e.,

$$F_{\perp} = p_w \begin{bmatrix} 0 \\ n_x \\ n_y \\ 0 \end{bmatrix} \tag{3.11.54}$$

The subscript w representing the values on the boundary. The variables other than the normal velocity such as the tangential velocity and thermodynamic properties

such as total enthalpy or entropy are to be obtained from the interior flow. Pressure p_w can be obtained either by solving the momentum equation or by extrapolating from the interior points. The former procedure will produce an artificial boundary layer . A zero order extrapolation implies that the pressure at the reference point itself is taken as the pressure at the boundary point, which is more justifiable in case of cell-vertex finite volume formulation.

Mirror boundary condition

In this condition the approximate Riemann solver used to determine the fluxes in the interior edges is also used on wall boundary. While calculating fluxes on the boundary, information regarding one of the state is obtained from interior state and the other state is determined in such a way that zero normal mass flux across the wall is guaranteed. There are various ways of determining the fictitious state. The fictitious velocity vector is obtained by reflecting the velocity vector computed on the wall.

The pressure p_f and density ρ_f in fictitious state are assigned the same values as in interior state. The mirror boundary condition can be represented as

$$u_{\perp f} = -u_{\perp I}, \quad u_{||f} = u_{||I}, \quad p_f = p_I, \quad \rho_f = \rho_I \tag{3.11.55}$$

where f and I refers to in fictitious state and interior state respectively. The main advantage of mirror boundary condition is that it permits the use of interior scheme (an approximate Riemann solver) on the wall boundary and thus it takes into direction of propagation. The drawback is, it does not take into account the effect of curvature and it is dissipative.

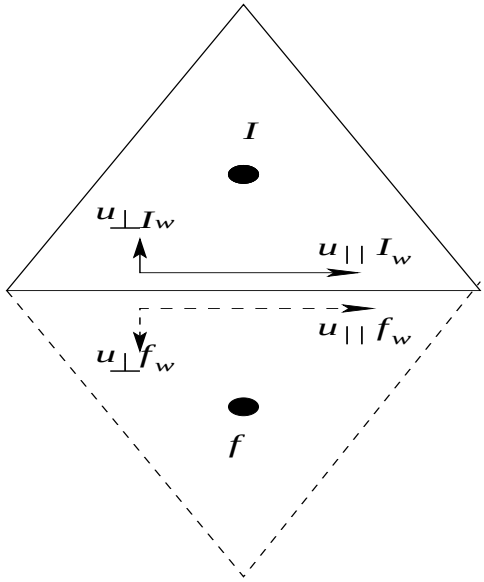

Figure 3.8: Mirror boundary condition

3.11.2 Viscous or no-slip boundary condition

For a viscous fluid which passes a solid wall, the relative velocity between surface and fluid is zero. In the case of stationary wall all the velocity components are zero. i.e.,

$$u = v = w = 0 \tag{3.11.56}$$

We can apply no-slip boundary conditions using dummy cell approach

$$u_{\perp f} = -u_{\perp I}, \quad u_{||f} = -u_{||I}, \quad p_f = p_I, \quad \rho_f = \rho_I \tag{3.11.57}$$

3.11.3 Farfield boundary condition

Detailed implementation of farfield boundary conditions are given in [24], [8]. Farfield boundaries are boundaries through which the flow enters or leaves the external flow field. In internal and external flow problems the inlet and outlet boundaries are assumed to be located far enough from the main flow region, and the influence of

the flow disturbances does not affect the freestream values. But high accuracy can be achieved when we make some corrections on the farfield. The usual way of implementing the farfield boundary conditions is using the information associated with the Riemann invariants, given by

$$R_1 = u_\perp + \frac{2c}{\gamma - 1} \qquad R_2 = u_\perp - \frac{2c}{\gamma - 1} \qquad R_3 = \frac{p}{\rho^\gamma} \tag{3.11.58}$$

These three Riemann invariants are associated with three waves with wave speeds of u+c, u-c and u respectively. They remain constant as they enter or exit the farfield. Depending on the value of the normal Mach number, Riemann invariants arriving at a face on the farfield are determined based on left and right states. From these Riemann invariants $u_\perp$, p, ρ etc are determined on the face. These values are used to find fluxes crossing the farfield.

3.11.4 Inflow/Outflow boundary conditions

Riemann invariants are calculated from known freestream values. So, farfield Boundary condition are well suited for external flows as freestream condition are known. It is not necessarily known all variables in case of internal flow. So, there is a separate treatment of boundary conditions are required in the case of internal flow problems

Inflow boundary condition

Supersonic flow

All the eigenvalues are positive, therefore all four variables are fixed by physical boundary conditions.

Subsonic flow

The direction normal to entry surface, Three eigenvalues are positive and one is negative. Therefore three quantities will have to be fixed by physical boundary

conditions, while remaining one will be determined by interior conditions, through numerical boundary condition.

Outflow boundary condition

Supersonic flow

All the eigenvalues are negative in sign, and no physical boundary conditions have to be given. All boundary values are extrapolated from interior flow.

Subsonic flow

Three eigenvalues are negative, three numerical boundary conditions have to be set, fourth one is specified by physical boundary conditions. The most appropriate boundary condition for internal flows are fixing the downstream static pressure.

The boundary conditions at inflow and outflow can be summarized as below

BC type	Physical BC	Numerical BC
Subsonic inflow	Three	One
Subsonic outflow	One	Three
Supersonic inflow	All 4 variables	None
Supersonic outflow	None	All 4 variables

Chapter 4

Code Validation

The inviscid as well as the viscous part of the solver is validated by comparing with various test cases results.
The inviscid code is validated for following test cases.

1. NACA 0012 airfoil

   (a) Flow with $M = 0.80$ and $\alpha = 1.25^o$

   (b) Flow with $M = 1.2$ and $\alpha = 0^o$

2. Bump in a channel problem

   Flow with $M = 0.85$ and $\alpha = 0.0^o$

3. Flow past a staggered-biplane configuration

   Flow with $M = 0.7$ and $\alpha = 0.0^o$

The viscous laminar flow code is validated for

1. Flow past a staggered-biplane configuration with $M = 0.8$, $\alpha = 10^o$ and $Re_\infty = 500$

For all cases relative residual fall is computed using following relation

$$Residue = maximum||\rho_i^n - \rho_i^{n-1}||/\rho_i^1 \quad 1 < i < nc \tag{4.0.1}$$

In entropy contours, entropy is calculated using (p/ρ_γ). C_p is calculated using formula

$$C_p = \frac{P_\infty - P}{0.5\rho_\infty u_\infty^2} \tag{4.0.2}$$

4.1 NACA 0012 airfoil

Two inviscid flow computations over the NACA 0012 airfoil have been performed to illustrate the performance of various schemes, reconstruction methods and limiters. Case1 : Transonic flow calculation for a freestream Mach number equal to 0.80 and 1.25^o angle of incidence has been carried out. Farfield is located 11 chords away from the airfoil. The flow geometry and the corresponding computational mesh is shown in Fig. 4.1. The generated grid consists of 11882 cells, 6028 points and 17910 faces.

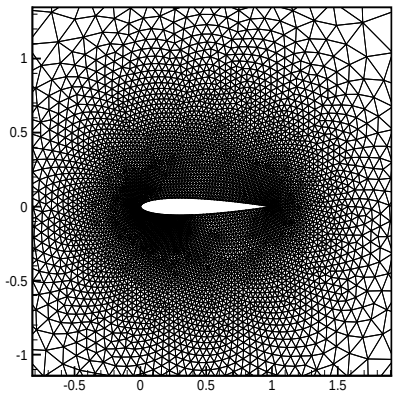

Figure 4.1: NACA 0012 airfoil grid pattern

The solution consists of an upper and lower surface shock wave and a trailing edge slip line. The pressure contours for 1st and 2nd order scheme are shown in Figs. 4.2(a) and 4.2(b) respectively. The solution obtained using piecewise constant reconstruction misses the lower surface shock and trailing edge slip line. The piecewise linear reconstruction method detects upper and lower surface shock waves as well as the slip line. It is well known that the high order scheme produces oscillations

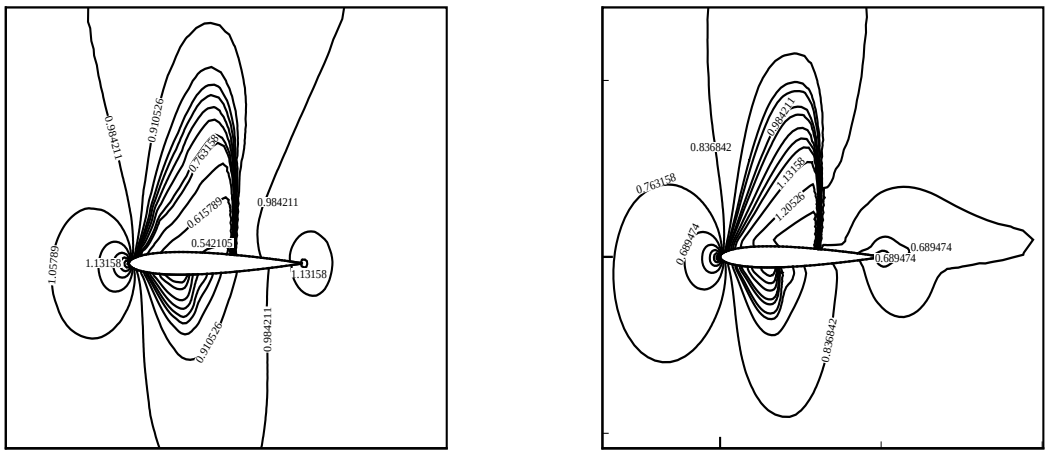

(a) Pressure contours for 1st order scheme (b) Pressure contours for 2nd order scheme

Figure 4.2: Pressure contours of flow over NACA 0012 airfoil problem ($M_\infty = 0.80, \alpha = 1.25^o$)

in the vicinity of discontinuities, which may even lead to instability. Figs. 4.3(c), 4.3(e) and 4.4(a) show the Cp oscillations near discontinuities for various 2nd order schemes with no-limiter. These oscillations are avoided by the use of limiters. Figs. 4.4(c) and 4.4(e) depict the oscillation free solution by employing limiters. Flux vector splitting schemes such as AUSM and AUSM+ are simple and robustness over existing schemes. Figs. 4.3(f) and 4.4(d) show that for the same accuracy level, the CPU time taken for inviscid computation is less in case of AUSM scheme than Roe scheme. Roe scheme is very accurate and particularly well suited for explicit upwind formulations. Nevertheless, the increased accuracy is accompanied with an increased operation count. From the various Cp results shown in Figs. 4.3 and 4.4, the performance of Roe scheme is intelligibly visible.

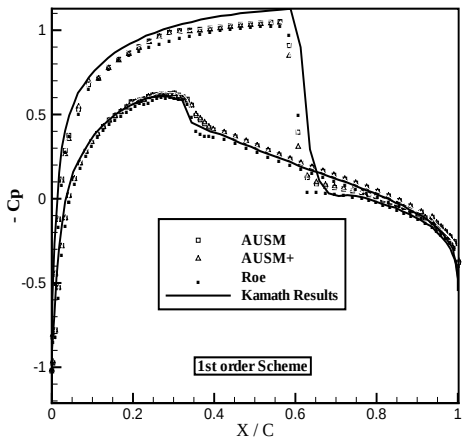

(a) Cp variation using 1st order scheme

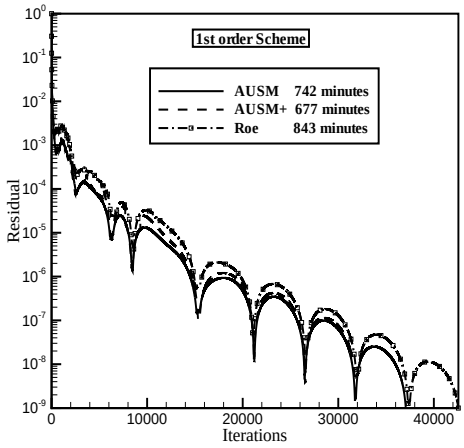

(b) Residual history for 1st order scheme

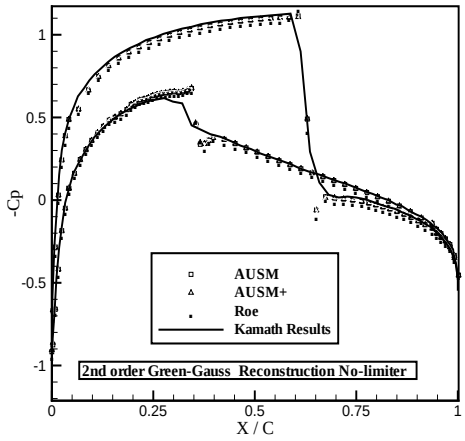

(c) Cp variation using 2nd order scheme (Green-Gauss reconstruction) with no limiter

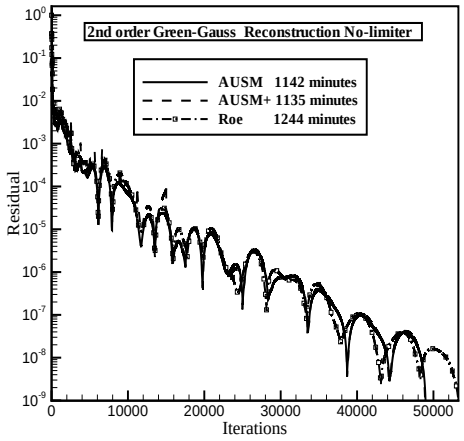

(d) Residual history for 2nd order scheme

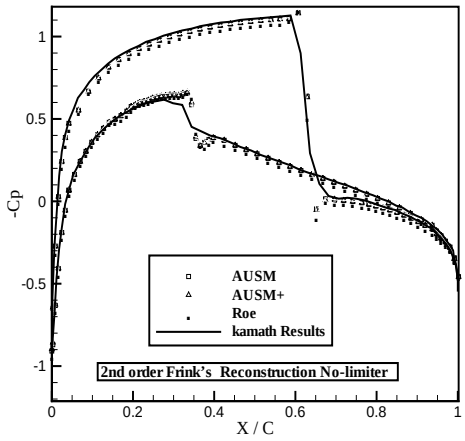

(e) Cp variation using 2nd order scheme (Frink's reconstruction) with no limiter

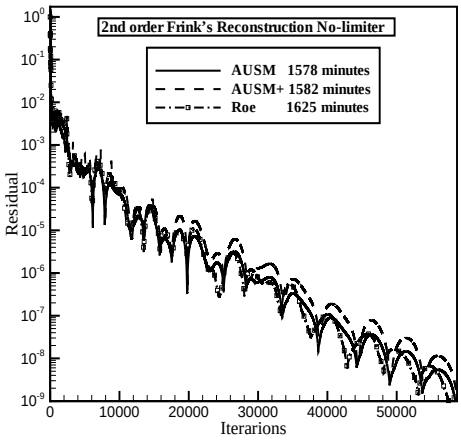

(f) Residual history for 2nd order scheme

Figure 4.3: Cp comparison of various schemes with no-limiter (Flow over NACA 0012 airfoil with $M_\infty = 0.80, \alpha = 1.25^o$)

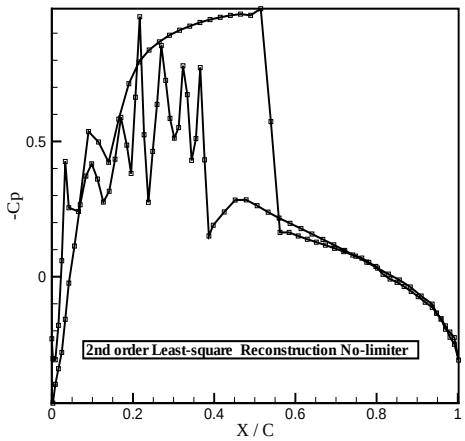

(a) Cp variation using 2nd order scheme (Roe scheme, Least-square reconstruction) with no limiter

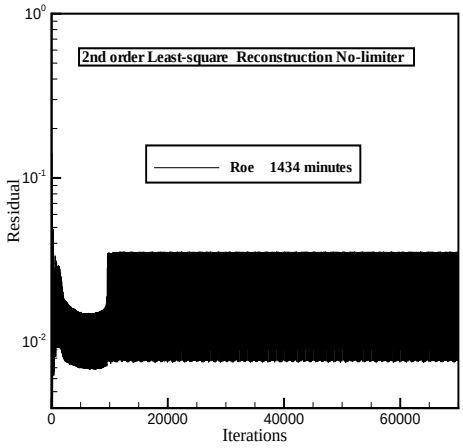

(b) Residual history for 2nd order scheme

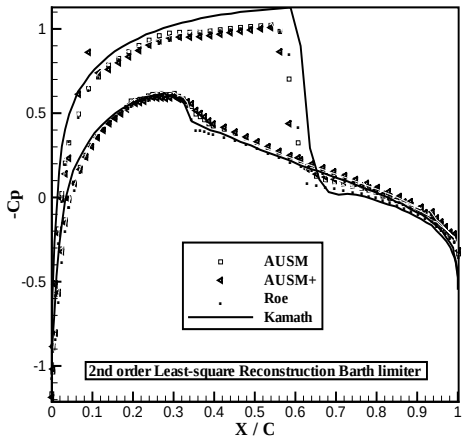

(c) Cp variation using 2nd order scheme (Least-square reconstruction) with Barth limiter

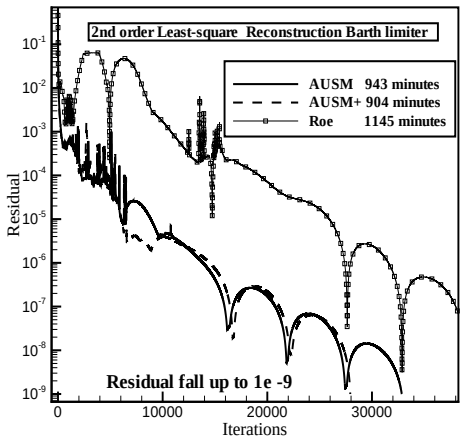

(d) Residual history for 2nd order scheme

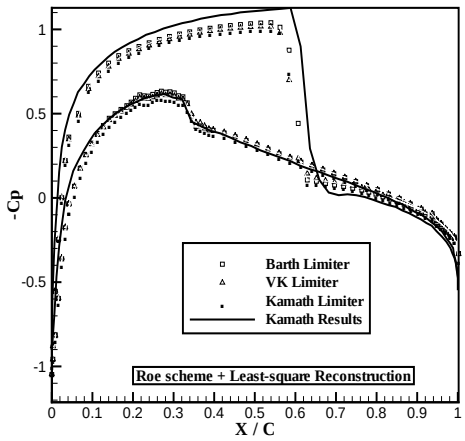

(e) Cp variation using Roe scheme with Least-square reconstruction

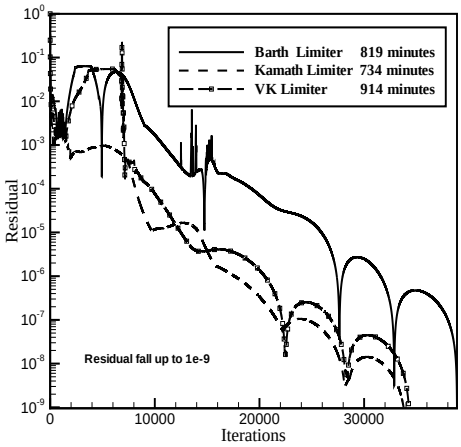

(f) Residual history for 2nd order scheme

Figure 4.4: Cp comparison of high order schemes with limiter (Flow over NACA 0012 airfoil with $M_\infty = 0.80, \alpha = 1.25^o$)

As expected the numerical solution is obtained by piecewise quadratic reconstruction is superior to the piecewise linear and constant reconstruction. Fig. 4.5(a) depicts that the quadratic reconstruction method captured both the upper and lower shocks are crisply. The surface pressure distribution for various order schemes are compared with Jawahar and Kamath [13] results and is shown in Fig. 4.5(b). Fig. 4.5(c) shows the residual history for various order scheme.

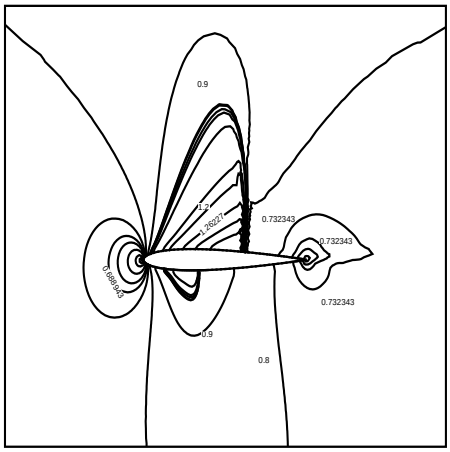

(a) Mach contours for 3rd order scheme

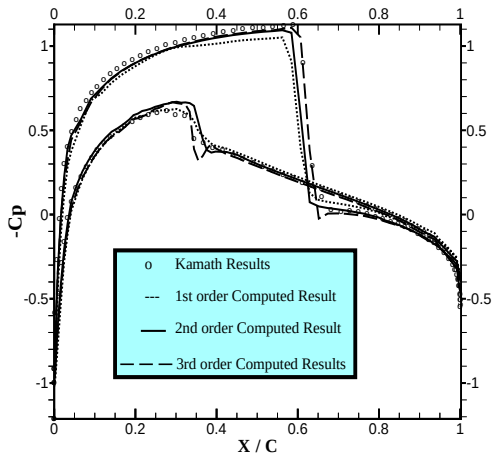

(b) Cp variation for various scheme

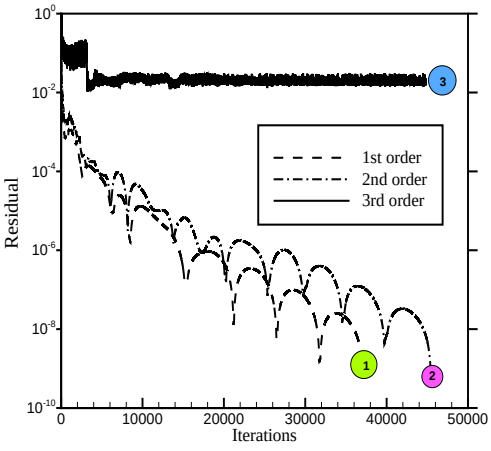

(c) Residual for various order scheme

Figure 4.5: Comparison of high order schemes for flow over NACA 0012 airfoil with $M_\infty = 0.80, \alpha = 1.25^o$

Case 2: Supersonic flow calculation for a freestream Mach number equal to 1.2 and 0^o angle of incidence has been carried out. Using the same grid pattern, the Mach contours and surface Mach distributions of second order scheme are shown in Figs. 4.6(a), 4.6(c). The excellent shock capturing quality of third order scheme is presented in Fig. 4.6(b). As compared to second order scheme, The third order scheme surface Mach distributions has good agreement with Delanaye [12] results. The residual history is shown in Fig. 4.6(d)

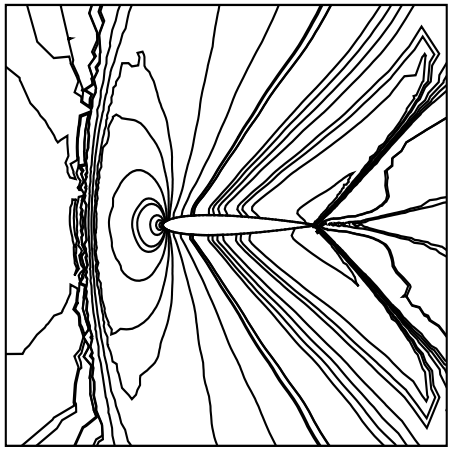

(a) Mach contours for 2nd order scheme

(b) Mach contours for 3rd order scheme

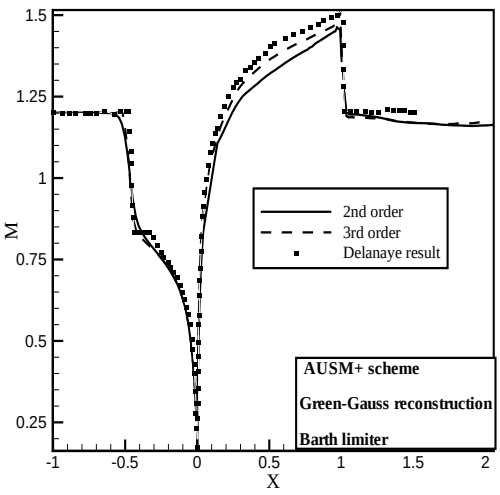

(c) Surface Mach distribution comparison

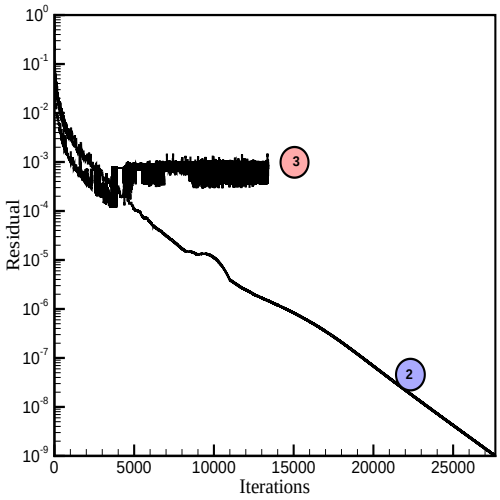

(d) residual history for 2nd and 3rd order scheme

Figure 4.6: Comparison high order schemes for flow over NACA 0012 airfoil problem with $M_\infty = 1.20, \alpha = 0^o$

4.2 Transonic flow over a bump in a channel

This is an internal flow through a channel having a 4.2% thick circular arc bump on its lower wall. The ratio of static downstream pressure to total upstream pressure corresponds to a Mach number of 0.85 in isentropic flow and the distance between the walls is 2.07 times the chord length of the bump. Total length of the channel is 5 times the chord length. The flow geometry and the corresponding computational mesh are shown in Figs. 4.7(a) and 4.7(b). The generated mesh consists of 28898 cells, 14669 points and 43566 faces.

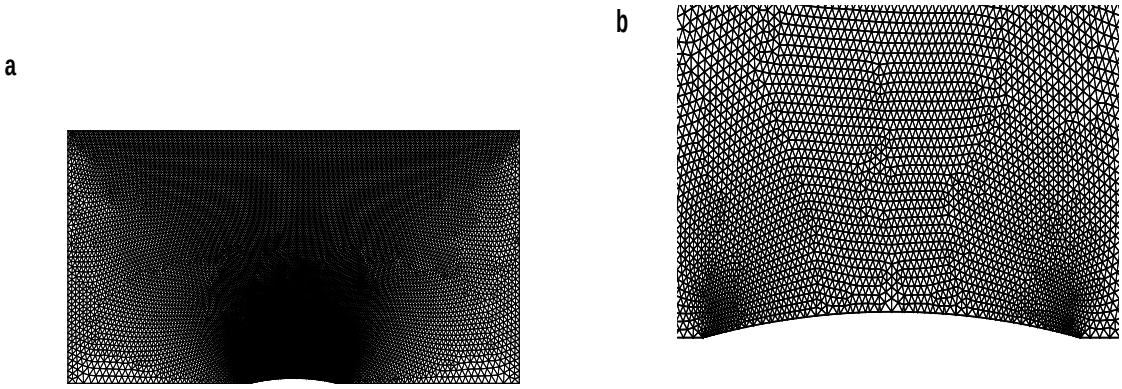

(a) Bump mesh (b) Closer view of bump

Figure 4.7: Bump in a channel mesh pattern

The lower wall, including the bump, and the top wall are modelled as being impermeable boundaries i.e., slip wall boundary condition is imposed. For computation, the second order scheme (Roe scheme, Green-Gauss reconstruction) with Barth limiter is used. The shock is created at 88.5% of the chord length from the leading edge and is very well captured on the body and in the flowfield. Fig. 4.8 shows the obtained pressure contours. Fig. 4.9 shows the pressure distribution along the lower wall. The computed Cp result is very well compared with the Liang and Chan [14] results. Residual history for 2nd order scheme is presented in Fig. 4.10.

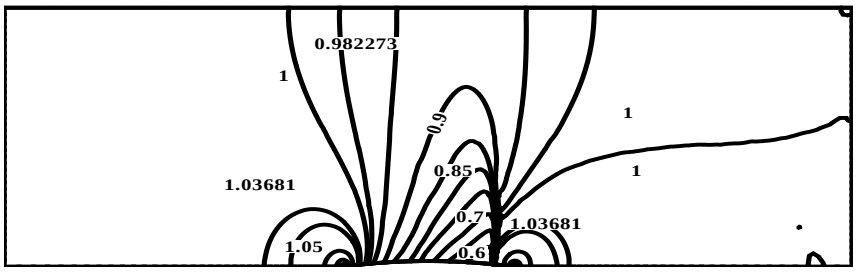

(a) Pressure contours

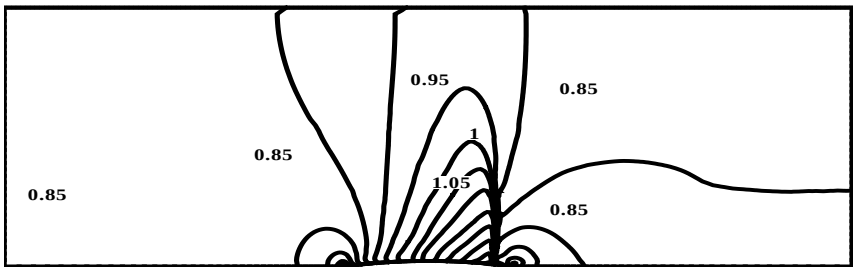

(b) Mach contours

Figure 4.8: Transonic channel flow $M_\infty = 0.85, t/c$ =4.2%

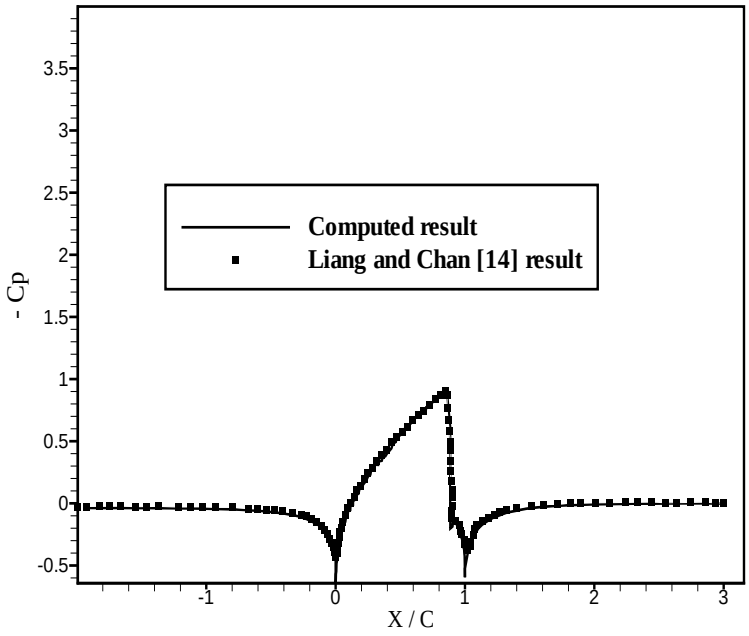

Figure 4.9: Comparison of pressure distributions along the lower wall for transonic bump in a channel flow $M_\infty = 0.85, t/c = 4.2\%$

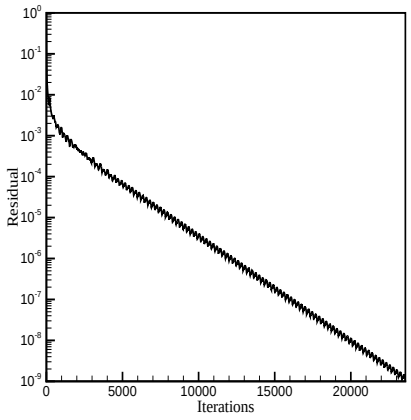

Figure 4.10: Second order residual history

4.3 Flow past a staggered-biplane configuration

The primary advantage of unstructured grids is their ability to straightforwardly account for multiple bodies in the flow. One of the popular test cases that is used for the purpose of demonstrating complex flow arising from interaction effects of multiple bodies is the staggered biplane [13]. It comprises two NACA 0012 airfoils, staggered by half a chord length in the pitchwise as well as chordwise direction. The resulting configuration yields a combination of internal as well as external flow as shown in Fig. 4.11, which depicts the unstructured coarse grid mesh with 110 points on each airfoil and with 8452 cells in the computational domain. The Mach number chosen is 0.7 with the flow being parallel to the chord of the airfoils. The second order scheme(AUSM+, LSQ reconstruction) with VK limiter is used for computation. Under these conditions an isolated NACA 0012 airfoil will yield a shock-free flow field whereas in the case of the staggered-biplane configuration the region between the airfoils acts as a channel which accelerates the flow. As a result of this flow confinement a strong normal shock is formed near the channel exit, which is depicted in Fig. 4.12.

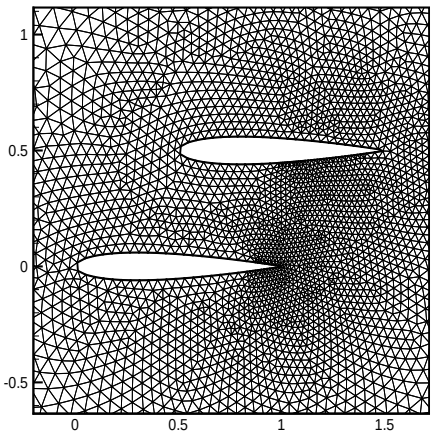

Figure 4.11: NACA 0012 biplane mesh

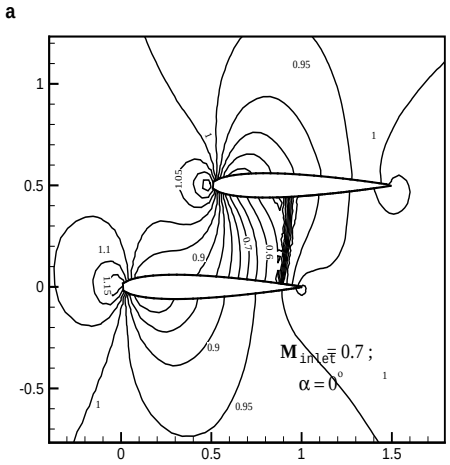

Figure 4.12: Pressure contours

Second order scheme (AUSM+, LSQ reconstruction) with VK limiter is used.

The accuracy of the solution not only depends on the schemes but also depends on the resolution of grid pattern. So the coarse grid pattern is refined to 45630 cells. Figs. 4.13(a) and (b) show the improved solutions after grid refinement. From Figs. 4.13(c) and (d), The computed 3rd order scheme surface pressure distributions are good agreement with Jawahar and kamath [13] results. Residual history is shown in Fig. 4.13(e). No convergence difficulty was observed for 2nd case even for a reduction in the residual up to 9 orders of magnitude.

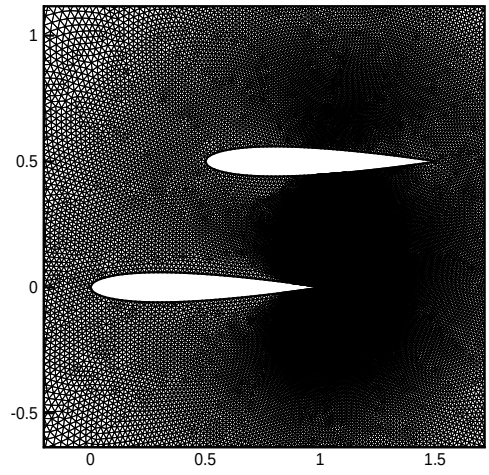

(a) Adaptively generated unstructured mesh

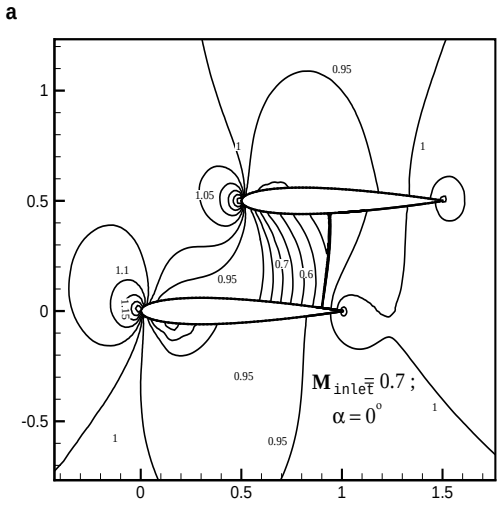

(b) Pressure contour

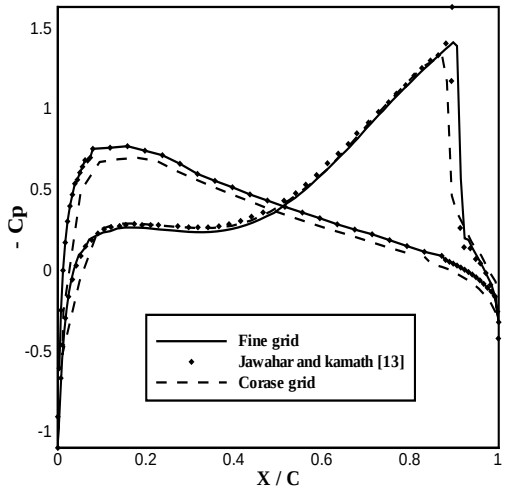

(c) Lower wall C_p variation

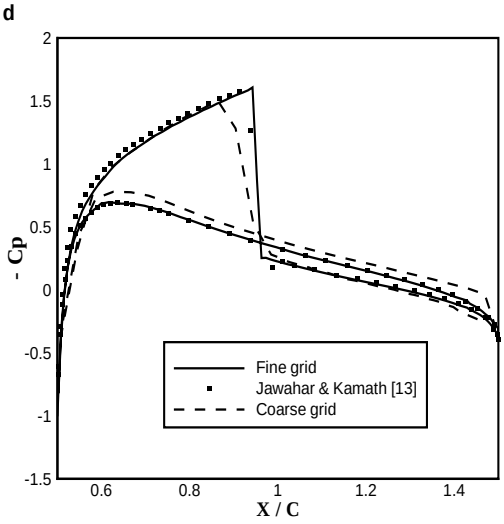

(d) Upper wall C_p variation

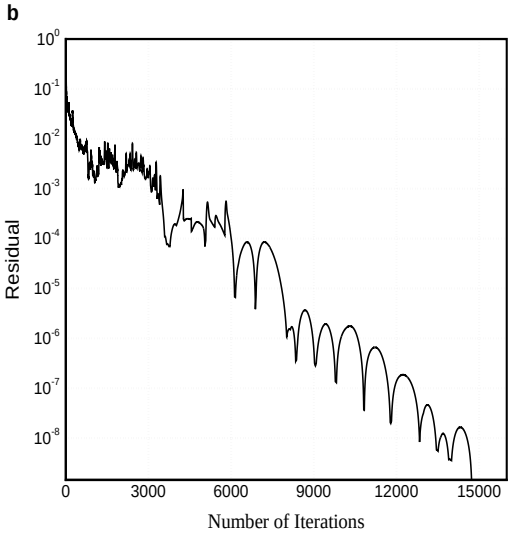

(e) Residual history

Figure 4.13: Adaptively generated mesh results $M = 0.7$, $\alpha = 0.00$

4.4 Viscous flow past a staggered-biplane configuration

The staggered NACA 0012 biplane configuration has been chosen for performing viscous flow computations. The grid, whose near-field view is shown in Fig. 4.14(a), contains 200 points on each airfoil with 35142 triangular cells in the computational domain. The flowfield disturbances generated by a lifting airfoil at transonic freestream Mach numbers extend outward to large distances from the airfoil. For the viscous computation, the outer boundary is a circle located 50 chord lengths from the airfoils. Freestream values are prescribed as farfield boundary conditions. streamlines corresponding to the flow parameters $M_\infty = 0.8, \alpha = 10^o, and\ Re_\infty = 500$ is shown in Fig. 4.14(b). The separated region on the upper surface of top airfoil reveals two vortices. As the secondary vortices are developed in the staggered plane configuration that does not appear in single airfoil viscous flow case, as cited by Jawahar and Kamath [13], it is evident that the secondary vortices are generated as an effect of the presence of a bottom airfoil. With the same logic, the flow separation on lower airfoil is completely avoided by presence of top airfoil. So this test case gives the taste of both internal and external viscous flow analysis. The Mach contours and pressure distributions have been plotted in Figs. 4.14(c) and (d) respectively. Although no experimental data or approved reference solutions are available for this test case, plausible viscous flow features have been captured with the low resolution unstructured-grid procedure. The 2nd order scheme residual history is shown in Fig. 4.14(e).

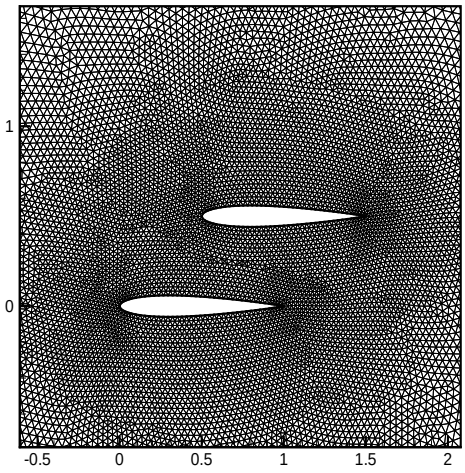

(a) Staggered biplane grid close view

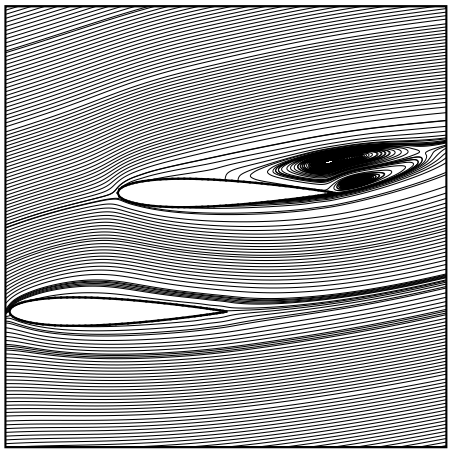

(b) Stream contours

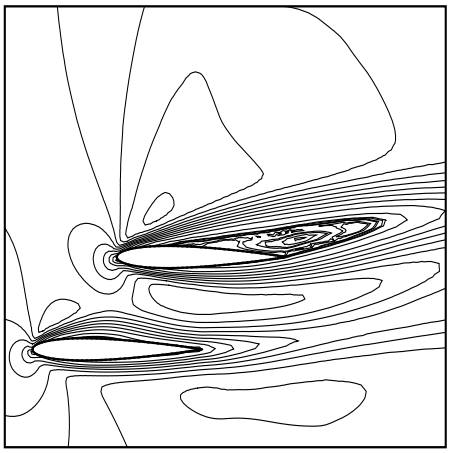

(c) Mach contours

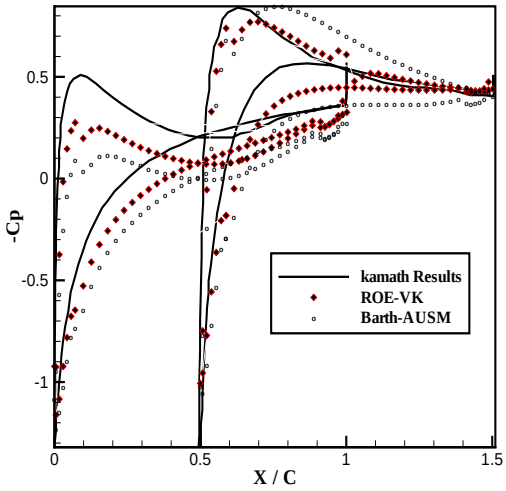

(d) Surface pressure distributions on airfoils

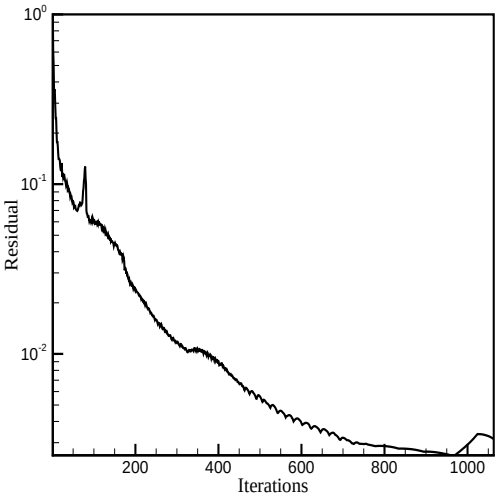

(e) Residual history

Figure 4.14: Viscous flow past staggered biplane airfoil 2nd order results $M_\infty = 0.8$, $\alpha = 10^o$, $Re_\infty = 500$

Chapter 5

Conclusions and Future Work

The accuracy of the Euler code has been extensively established by comparing with various test cases. The accuracy of viscous code is ensured and plausible viscous flow features have been captured with high resolution. Third order scheme is constructed and tested for the Euler equations for the arbitrary unstructured meshes. The properties of various schemes, reconstruction methods and limiters are studied.

Barth limiter faces convergence problems in most of the flow conditions. Venkatakrishnan limiter is comparatively good. But some preliminary work is required in selection of the parameters to get monotonic and converged solutions. Jawahar and Kamath limiter also displays good convergence properties. However, it is not very good at weak shocks compare to the other two limiters.

5.1 Scope for future work

1. The solver can be extended for incompressible computations by employing low Mach number preconditioning for unstructured schemes.

2. The code can be extended to turbulence computations by adding a suitable

algebraic turbulent model to it.

3. In order to drastically decrease the computational time, the mode of computation can be altered to implicit.

Bibliography

[1] Jameson, A. and Mavriplis, D. J. Finite Volume Solution of Two-Dimensional Euler Equations on Regular Triangular Mesh, *AIAA Journal*, **24**. No. 4, pp.611-618, April 1986.

[2] Godunov, S.K. A Differnce Scheme for Numerical Computation of Discontinuous Solution of Hydrodynamic Equations, Math. Sbornik, **47**, pp. 271-306, 1959 (in Russian).

[3] Roe, P. L. Approximate Riemann Solvers, Parameters Vectors and Difference Schemes. *J. Computational Physics*, **43**, pp.357-372, 1981.

[4] Steger, J. L. and Warming R. F. Flux Vector Splitting of Inviscid Gas-Dynamic Equations with Application to Finite Differeence Methods, 1981.

[5] van Leer, B., Towards the Ultimate Conservative Difference Schemes Monotonicity and Conservation Combined in Second Order Scheme. *J. Computational Physics*, **14**, pp.361-370, 1979.

[6] Liou, M. S. and Stefen, C. J. Jr. A New Flux Splitting Scheme, *J. Computational Physics*, **107**, 1993, pp. 23-39, 1981.

[7] Liou, M. S. A sequel to AUSM: AUSM+, *J. Computational Physics*, 1993 **129**, pp. 364-382, 1981.

[8] Jameson, A. Solutions of the Euler Equations for Two-Dimensional Transonic Flow by a Multigrid Method. MAE report No.1613, 1983.

[9] Barth T. J. and Dennis C. Jaspersen. The Design and Application of Upwind Schemes on Unstructured Meshes, *AIAA 89-0366*, Jan. 1989.

[10] Barth T. J. and Paul O. Frederickson. Higher Order Solution of the Euler Equations on Unstructured Grids Using Quadratic Reconstruction, *AIAA-90-0013*, January 8-11, 1990/Reno, Nevada.

[11] Barth T. J. Recent Developments in High Order K-Exact Reconstruction on Unstructured Meshes, *AIAA-93-0668*, January 11-14, 1993/Reno, Nevada.

[12] Delanaye M. and Essers J. A. Quadratic-Reconstruction Finite Volume Scheme for Compressible Flows on Unstructured Adaptive Grids, *AIAA*, **35**, No. 4, April 1997.

[13] Jawahar, and Hemanth Kamath P., A High Resolution Procedure for Euler and Navier-Stokes Computations on Unstructured Grids, *J.Computational Physics*, **164**, pp. 165-203, 2000.

[14] Liang S, and Chan J., An Improved Upwind Scheme for the Euler Equations, *J.Computational Physics*, **84**, pp. 461-473, 1989.

[15] Courant, R., Isaacson, E. and Rees, M. On solution of Non-linear Hyperbolic Differential Equations by Finite Differences, *Cpmm.Pure and Applied Mathematics*, **5**, pp. 243-255, 1952.

[16] Jameson. A. Artificial Diffusion, Upwind Biasing, Limiters and Their Effect on Accuracy and Multigrid Convergence in Transonic and Hypersonic Flow *AIAA Paper 93-3559*, 1982.

[17] Osher, S. and Solomon, F. Upwind Difference Schemes for Hyperbolic System of Conservation Laws, *Math. Comp.*, **38**, pp. 339-374, 1982.

[18] Blazek, J. Computational Fluid Dynamics: Principles and Applications, Elsevier, 2001.

[19] Venkatakrishnan, V. Prespective on Unstructured Grid Flow Solvers, icase-1995-3.

[20] Frink, N. T. Upwind Scheme for Solving the Euler Equations on Unstructured Tetrahedral Meshes, *AIAA Journal*, **30**, No.1, pp.70-77.

[21] Venkatakrishnan, V. Convergence to Steady State Solutions of the Euler Equations on Unstructured Grids with Limiters, *J. Computaional Physics*, **118**, 120-130,1995.

[22] Rosendale, J. V. Floating shock Fitting via Lagrangian Adaptive Meshes, *ICASE 94-89*, 1989.

[23] Jameson, A., Schmidt, W. and E.Turket, Numerical Simulation of the Euler Equations by Finite Volume Methods Using Runge-Kutta Time Stepping Schemes, *Pres.at the 5th AIAA comput.Flu.Dyn.conf. AIAA-81-1259*, 1981.

[24] Charles Hirsh., Numerical Computation of Internal and External Flows, Vol 1 and 2, Wiley, Newyork, 1998.

[25] Bala Krishnan, N. Fernandez, G. Wall Boundary Conditions for Inviscid Compressible Flows on Unstructured Meshes, *Int.J. Numer.Meth.Fluids*, **28**, pp.1481-1501, 1998.